JCB Journal of Cell Biology

ARTICLE

Integrated control of formin-mediated actin assembly by a stationary inhibitor and a mobile activator

Mikael V. Garabedian[1], Tatiana Stanishneva-Konovalova[2], Chenyu Lou[1], Thomas J. Rands[1], Luther W. Pollard[1], Olga S. Sokolova[2], and Bruce L. Goode[1]

Formins are essential actin assembly factors whose activities are controlled by a diverse array of binding partners. Until now, most formin ligands have been studied on an individual basis, leaving open the question of how multiple inputs are integrated to regulate formins in vivo. Here, we show that the F-BAR domain of *Saccharomyces cerevisiae* Hof1 interacts with the FH2 domain of the formin Bnr1 and blocks actin nucleation. Electron microscopy of the Hof1–Bnr1 complex reveals a novel dumbbell-shaped structure, with the tips of the F-BAR holding two FH2 dimers apart. Deletion of Hof1's F-BAR domain in vivo results in disorganized actin cables and secretory defects. The formin-binding protein Bud6 strongly alleviates Hof1 inhibition in vitro, and *bud6Δ* suppresses *hof1Δ* defects in vivo. Whereas Hof1 stably resides at the bud neck, we show that Bud6 is delivered to the neck on secretory vesicles. We propose that Hof1 and Bud6 functions are intertwined as a stationary inhibitor and a mobile activator, respectively.

Introduction

Formins are a conserved family of actin assembly-promoting proteins with wide-ranging biological roles and remarkable biochemical properties. In mammals, there are 15 different formin genes, which play critical roles in several actin-based processes, including cell motility, intracellular transport, cytokinesis, and cell and tissue morphogenesis (Faix and Grosse, 2006; Chhabra and Higgs, 2007). Formins are large multidomain proteins with a modular design. The N-terminal half of formins directs their localization in cells and contributes to their regulation. The C-terminus contains unstructured proline-rich FH1 domains that recruit profilin-bound actin monomers and a dimeric donut-shaped FH2 domain that directly nucleates actin assembly. The FH2 domain remains processively attached to the growing barbed end of the filament, accelerating elongation in concert with the FH1 domains and profilin, and antagonizing capping protein (Kovar, 2006; Goode and Eck, 2007; Breitsprecher and Goode, 2013).

Because formins have such strong effects in promoting actin assembly, their activities must be tightly controlled in vivo. This is mediated in part by several ligands with diverse effects on formin activities (Chesarone et al., 2010; Breitsprecher and Goode, 2013). For instance, the F-BAR protein CIP4/Toca-1 binds to the FH1 domain of Dia1 to inhibit actin assembly, and the F-BAR protein SrGAP2 binds to the FH1 domain of FMNL1 to inhibit actin severing (Mason et al., 2011; Yan et al., 2013). Furthermore, DIP/WISH binds to the FH2 domain of Dia2 to inhibit actin assembly (Eisenmann et al., 2007). In contrast, adenomatous polyposis coli (APC) protein and Spire bind to the C-terminal tails of formins to enhance actin nucleation (Okada et al., 2010; Breitsprecher et al., 2012; Quinlan, 2013), and CLIP-170 binds to the FH2 domain of formins to further accelerate actin elongation (Henty-Ridilla et al., 2016). In each case, these proteins have been studied individually for their effects on formins, leaving a major gap in our understanding of how inputs from multiple ligands are integrated to control formin activity in vivo.

Saccharomyces cerevisiae expresses only two formins, Bni1 and Bnr1. Throughout the cell cycle, formins assemble linear actin cables, which serve as polarized tracks for the transport of post-Golgi secretory vesicles, organelles, and other cargoes to the growing daughter cell (bud; Moseley and Goode, 2006). Bni1 and Bnr1 are genetically redundant and polymerize complementary sets of cables that grow rapidly from the bud tip and neck, respectively, at ∼0.3–0.7 µm/s (Evangelista et al., 2002; Pruyne et al., 2002, 2004; Sagot et al., 2002a,b; Yang and Pon, 2002;

[1]Department of Biology, Rosenstiel Basic Medical Science Research Center, Brandeis University, Waltham, MA; [2]Bioengineering Department, Faculty of Biology, Lomonosov Moscow State University, Moscow, Russia.

Correspondence to Bruce L. Goode: goode@brandeis.edu.

Buttery et al., 2007; Yu et al., 2011). Bni1 assembles cables that fill the bud and extend into the mother cell, whereas Bnr1 is stably anchored at the bud neck to septins (Gao et al., 2010; Buttery et al., 2012) and assembles cables that specifically fill the mother compartment. Transport of post-Golgi secretory vesicles along cables is driven by the essential type V myosin, Myo2, at ∼3 µm/s (Schott et al., 1999, 2002). When cable assembly is shut off by fast-acting temperature-sensitive formin mutants, secretion and cell growth arrest (Evangelista et al., 2002; Sagot et al., 2002a), demonstrating that continuous polymerization of cables is essential for polarized cell growth.

In yeast, the ability of formins to produce dynamic actin cables of the appropriate length, architecture, and organization requires inputs from diverse formin-binding partners. Bud6 is a polarity factor required both for maintaining normal levels of cable assembly and facilitating microtubule capture at the bud cortex to facilitate spindle orientation (Amberg et al., 1997; Evangelista et al., 1997; Segal et al., 2000; Huisman et al., 2004; Ten Hoopen et al., 2012). Purified Bud6 binds to actin monomers and enhances both Bni1- and Bnr1-mediated actin nucleation, and Bud6 interactions with formins and G-actin are critical for its in vivo functions in cable assembly (Moseley and Goode, 2005; Graziano et al., 2011, 2013). Bud14 binds to the FH2 domain of Bnr1, displacing it from growing ends of filaments, and *bud14* mutants contain overgrown cables (Chesarone et al., 2009; Eskin et al., 2016). Smy1 also binds to the FH2 domain of Bnr1 and induces pausing of actin filament elongation, controlling cable growth rates and length in vivo (Chesarone-Cataldo et al., 2011; Mohapatra et al., 2015). Interestingly, Smy1 is on secretory vesicles, and trafficked on cables to the bud neck, where vesicles pause for 1–3 s before moving into the bud. As such, Smy1 is a mobile inhibitor component of a cable-length–dependent negative feedback loop preventing overgrowth (Mohapatra et al., 2015; Eskin et al., 2016). Hof1 is an F-BAR protein that colocalizes with Bnr1 at the bud neck and inhibits actin assembly by Bnr1 (Graziano et al., 2014). Although each formin-binding protein has unique biochemical effects and makes a unique genetic contribution to maintaining normal cable structure and function, it is still not understood how these different inputs are coordinated in vivo to tune formin activity.

In this study, we uncover a formin regulatory mechanism that integrates the potent inhibitory effects by Hof1 with a novel activation role for Bud6. Hof1 localizes to the bud neck, where it has important roles in cytokinesis (Kamei et al., 1998; Vallen et al., 2000; Blondel et al., 2005; Nishihama et al., 2009; Meitinger et al., 2011, 2013; Nkosi et al., 2013; Wang et al., 2018). However, we previously showed that Hof1 also functions earlier in the cell cycle in regulating Bnr1 during polarized cell growth (Graziano et al., 2014). We demonstrated that the C-terminal SH3 domain of Hof1 inhibits the activities of the FH1 domain of Bnr1 to tune cable organization and function. However, the effects of full-length (FL) Hof1 were not examined, leaving the functions of the N-terminal F-BAR domain a mystery. F-BAR domains are best known for binding membranes and sensing or stabilizing membrane curvature (McDonald and Gould, 2016). Indeed, a recent structural study demonstrated that Hof1's F-BAR domain forms a crescent-shaped dimer that binds lipids in vitro (Moravcevic et al., 2015). However, the F-BAR domain of Hof1 is not required for its localization to the bud neck in vivo; instead, this is mediated by an adjacent coiled-coil domain (CC2) that binds septins (Oh et al., 2013). It has remained an open question what functions might be performed by Hof1's F-BAR domain in vivo.

Here, we isolate Hof1-FL and show that it is a potent inhibitor of Bnr1-mediated actin nucleation (K_{app} ∼1.4 nM) and that the F-BAR domain directly inhibits the FH2 domain. Using single-particle EM, we define the structure of the Hof1–Bnr1 complex, revealing a unique architecture in which the tips of the F-BAR dimer appear to obstruct key actin-binding surfaces on the FH2 domain. Bud6 overcomes inhibition by Hof1 to trigger Bnr1-mediated actin assembly in vitro, and in vivo, we find that Bud6 is on secretory vesicles, transported along cables to the neck. We propose a model in which the roles of a stationary inhibitor (Hof1) and a mobile activator (Bud6) are integrated to spatially and temporally control formin-mediated actin assembly.

Results

Hof1-FL potently inhibits Bnr1-mediated actin assembly

Previously, we defined the activities of the C-terminal half of Hof1 (Hof1-CT; 350–669) and found that the SH3 domain of Hof1 binds to the FH1 domain of Bnr1, resulting in partial inhibition of actin assembly (Graziano et al., 2014). Further, a deletion of the C-terminal half of Hof1 (*hof1ΔCT*) caused modest defects in actin cable organization and function in vivo. However, we noted that cable defects were more pronounced in *hof1Δ* compared with *hof1ΔCT* cells, suggesting that the N-terminal half of Hof1 may contribute, directly or indirectly, to cable regulation.

Here, we addressed this issue by isolating Hof1-FL and three different fragments of the N-terminus (NT; F-BAR and CC2; Fig. 1, A and B) and testing their effects on C-Bnr1 (FH1, FH2, and tail domains) in bulk actin assembly assays. Hof1-FL displayed potent, concentration-dependent inhibition of C-Bnr1 activity, with half-maximal inhibition (of 2 nM C-Bnr1) at 1.4 nM Hof1-FL (Fig. 1, C and D). This K_{app} was ∼100-fold stronger than the K_{app} for Hof1-CT, which was artificially dimerized to mimic the presumptive dimeric state of the FL protein (Graziano et al., 2014). Hof1-NT alone inhibited C-Bnr1 (Fig. 1 D) with reduced potency (K_{app} ∼0.58 µM) compared with Hof1-FL, and was able to inhibit the Bnr1 FH2 domain alone with similar potency (K_{app} ∼0.68 µM; Fig. 1 D). This inhibitory effect differs from Hof1-CT, which inhibits Bnr1 by targeting the FH1 domains. The combination of Hof1's F-BAR domain interacting with the FH2 domain and its SH3 domain interacting with the FH1 domain make Hof1-FL an extremely potent inhibitor of Bnr1.

To better understand Hof1's inhibitory effects on Bnr1, we used total internal reflection fluorescence (TIRF) microscopy to observe the dynamics of individual actin filaments (Fig. 1 E). C-Bnr1 induced the formation of numerous filaments compared with control reactions containing actin and profilin without formin (Fig. 1, E and F), and as expected, these filaments elongated at an accelerated rate (Fig. 1 G). Addition of Hof1-FL blocked the nucleation effects of C-Bnr1 (Fig. 1, E and F) but showed no effect on actin assembly in the absence of formin and minimal effect on the activity of C-Bni1 (Fig. S1). Hof1-NT also inhibited

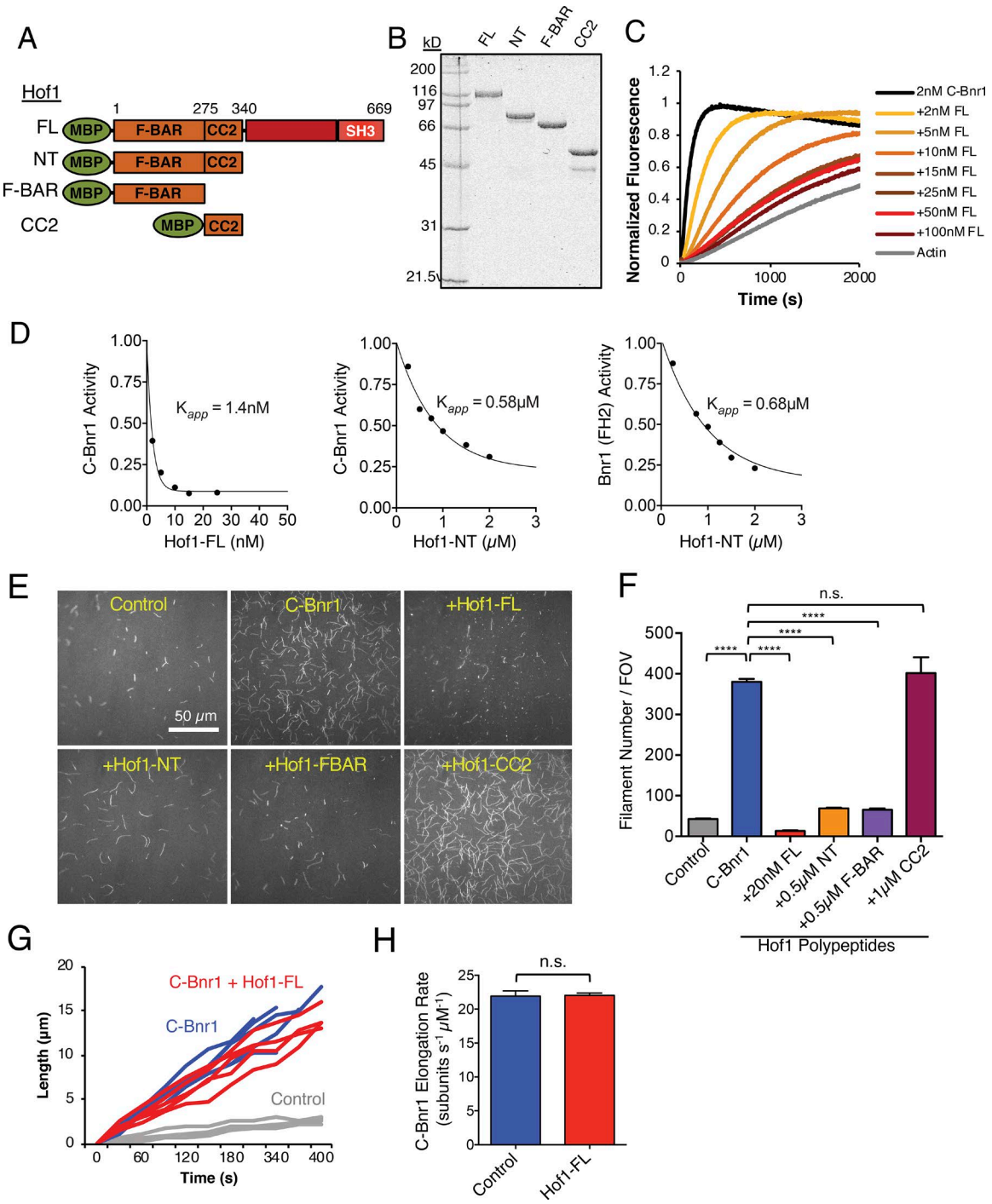

Figure 1. **Hof1-FL is a potent inhibitor of Bnr1-mediated actin nucleation. (A)** Schematic of Hof1 constructs purified. CC2, coiled-coil 2 domain; F-BAR, FCH Bar-Amphiphysin-Rvs domain; MBP, maltose-binding protein; SH3, Src homology 3 domain. **(B)** Coomassie-stained SDS-PAGE gel of purified MBP-tagged Hof1 polypeptides (100 ng each). **(C)** Inhibitory effects of Hof1-FL on C-Bnr1–mediated actin assembly. Reactions contain 2 µM actin monomers (5% pyrene labeled), 2 nM C-Bnr1 (FH1-FH2-C), and indicated concentrations of Hof1-FL (0–100 nM). **(D)** Concentration-dependent effects of Hof1-FL or Hof1-NT on 2 nM C-Bnr1 or Bnr1 (FH2), as indicated; data from assays as in C. **(E)** TIRF microscopy analysis showing the effects of different Hof1 polypeptides on C-Bnr1. Reactions contained 0.5 µM actin monomers (10% OG labeled; 0.5% biotin-actin), 3 µM yeast profilin, 0.2 nM C-Bnr1, and concentrations of Hof1 polypeptides indicated in F. Images are from 300 s after initiation of actin assembly. Bar, 50 µm. **(F)** Quantification of actin filament nucleation from TIRF assays as in E. Data are averaged from four FOVs in each of two independent experiments (eight FOVs total). Error bars represent SEM. Statistical significance calculated by one-way ANOVA (n.s., not significant; ****, $P \le 0.0001$). **(G)** Example traces of individual elongating actin filaments (five each) from TIRF assays as in E. **(H)** Elongation rates quantified from two independent TIRF experiments. Filaments were first polymerized with C-Bnr1, and then Hof1-FL or control buffer was flowed in, with 3 µM profilin and 0.5 µM actin monomers ($n = 10$ filaments per condition). Error bars represent SEM. Statistical significance calculated by unpaired *t* test (n.s., not significant).

C-Bnr1 nucleation activity in TIRF assays, as did the F-BAR domain construct (1–275; Fig. 1 F). In contrast, the remaining portion of the NT, or CC2 domain (276–340), had no effect. These results suggest that the F-BAR domain of Hof1 directly inhibits C-Bnr1–mediated actin nucleation.

Analysis of elongation rates revealed fast-growing actin filaments in TIRF reactions containing C-Bnr1 (Fig. 1 G). Reactions containing C-Bnr1 and Hof1-FL had many fewer filaments, consistent with inhibition of Bnr1-mediated nucleation, but contained a small number of fast-growing filaments. This observation raises the possibility that once a filament is successfully nucleated by C-Bnr1, its accelerated elongation by C-Bnr1 is not affected by Hof1-FL (Fig. 1 G). To test this more directly, we first polymerized filaments using C-Bnr1 and profilin, at the accelerated rate, and then flowed in Hof1-FL or control buffer (each including profilin and actin monomers). Adding Hof1-FL to filaments being polymerized by C-Bnr1 did not alter their elongation rates (Fig. 1 H), suggesting that Hof1 specifically regulates Bnr1-mediated nucleation.

Structure of the Hof1–Bnr1 complex

To gain structural insights into Hof1 inhibition of Bnr1, we used negative staining and single-particle EM to examine the complex formed by Hof1-FL and C-Bnr1. C-Bnr1 dimers alone appeared as donut-shaped structures (Fig. 2 A), consistent with the FH2 crystal structure (Xu et al., 2004). Further, Hof1-FL dimers (and F-BAR domain dimers) had an elongated crescent-shaped appearance (Figs. 2 A and S2 A), consistent with the Hof1 F-BAR crystal structure (Moravcevic et al., 2015). When combined, Hof1-FL and C-Bnr1 formed a novel "dumbbell" structure, ∼25 nm in length, with two donut-shaped densities held apart by the tips of an elongated rod (most abundant class averages in Fig. 2 B). In raw EM images, we could see the N-terminal MBP tags on Hof1-FL as globular masses in variable orientations sprouting from the elongated Hof1-FL dimer. Therefore, these extra masses were averaged out and do not appear in the class averages. Bnr1 FH1 domains and C-terminal tails were not visible in our raw images, likely because they are unstructured and lack sufficient density (Maiti et al., 2012).

Using the random conical tilt method on 4,650 particles, we generated a 10-Å resolution 3D reconstruction, into which we docked the crystal structures of the Hof1 F-BAR dimer and two FH2 dimers by an automated analysis (Figs. 2 C and S2 D). The molecular architecture of the complex suggests that a single Hof1-FL dimer binds to two C-Bnr1 dimers and that the FH2 domains contact the tips of the elongated Hof1 dimer. We also solved the structure of a lower-molecular-weight complex consisting of the Hof1 F-BAR domain (1–275) bound to two Bnr1 FH2 domains (lacking FH1 domains or C-terminal tails). From 3,500 particles, we generated a 24 Å resolution 3D reconstruction (Figs. 2 D and S2 B). This structure had an overall shape and arrangement similar to the higher-molecular-weight complex but with less mass, as indicated by the difference map (Fig. S2 D). In the lower-molecular-weight complex, there also was greater variability in the positions of the FH2 dimers, suggesting that this complex may be less rigid, possibly due to the absence of SH3 domain interactions with FH1 domains. Crystal structures of the F-BAR and FH2 domain were automatically docked into the higher-molecular-weight complex formed by Hof1-FL and C-Bnr1 and yielded high-confidence fits (Fig. S2 C). Docking indicates that the tips of the F-BAR dimer contact the FH2 domain near its linker region, which connects the two halves of the FH2 dimer (Xu et al., 2004). This puts the F-BAR tips extremely close to key actin-binding surfaces on the FH2 domain (Fig. 2 E), suggesting that the F-BAR domain obstructs actin binding to inhibit nucleation. In our structure of Hof1-FL bound to C-Bnr1, the locations of the SH3 domains are difficult to pinpoint, but based on difference mapping, they may correspond to either of the two pairs of extra masses adjacent to the FH2 domains (Fig. S2 D).

Loss of the F-BAR domain of Hof1 results in aberrant actin cable networks

We next asked how loss of the F-BAR domain of Hof1 affects actin cable assembly in vivo by integrating a deletion of the F-BAR domain of Hof1 (*Δ2-275*; or *hof1ΔFBAR*) and examined cellular actin organization. Importantly, deletion of the F-BAR domain did not affect localization or levels of Hof1 at the neck (Fig. S3, A and B). A previous study showed that deletion of a larger portion of the NT (1–300) partially impairs neck localization (Meitinger et al., 2011), suggesting that sequences immediately C-terminal to the F-BAR domain contribute to localization.

Wild-type, *hof1ΔFBAR*, and *hof1Δ* cells were fixed and compared for F-actin organization using structured illumination microscopy (SIM; Fig. 3 A). Deletion of *HOF1* or the F-BAR domain resulted in disorganized actin cable networks in mother cells. Cable organization was quantified by SOAX (Xu et al., 2015), an open-source program for quantitatively assessing polymer networks (Fig. 3, B and C). Both *hof1Δ* and *hof1ΔFBAR* cells had higher numbers of cable segments and intersections than wild-type cells (Fig. 3, D and E), consistent with excessive cable assembly and entanglement (disorganized cables that cross more frequently). Unfortunately, we were unable to quantify cable numbers or lengths in *hof1Δ* cells because of their disorganization and crossovers. Cables in the mutants were also improperly aligned with respect to the mother-bud axis compared with cables in wild-type cells (Fig. 3 C). We also treated cells for 10 min with the Arp2/3 complex inhibitor CK666 to remove actin patches and thus obtain improved views of cable organization (Fig. S3 C; Nolen et al., 2009; Burke et al., 2014). We used coefficient of variation (CV; or standard deviation/mean intensity) analysis of cable staining in CK666-treated cells as a metric for cable organization in the mother compartment. Wild-type cells had a higher CV than mutants due to having fewer cables (bright pixels) surrounded by more dark background regions (dark pixels). *hof1Δ* and *hof1ΔFBAR* mutants both had lower CV values, consistent with more dispersed and disorganized cables (Fig. 3 F).

Further, we asked whether the disorganized cables in *hof1ΔFBAR* and *hof1Δ* cells affect secretory traffic by monitoring the movements of post-Golgi vesicles marked with GFP-Sec4 in mother cells (Eskin et al., 2016). The paths of vesicle movements were traced in ImageJ (representative traces in Fig. 3 G) to measure path length, and we determined path tortuosity (i.e., the ratio of the length of a path to the distance between its point of origin and the bud neck). Vesicle paths were longer (Fig. 3 H)

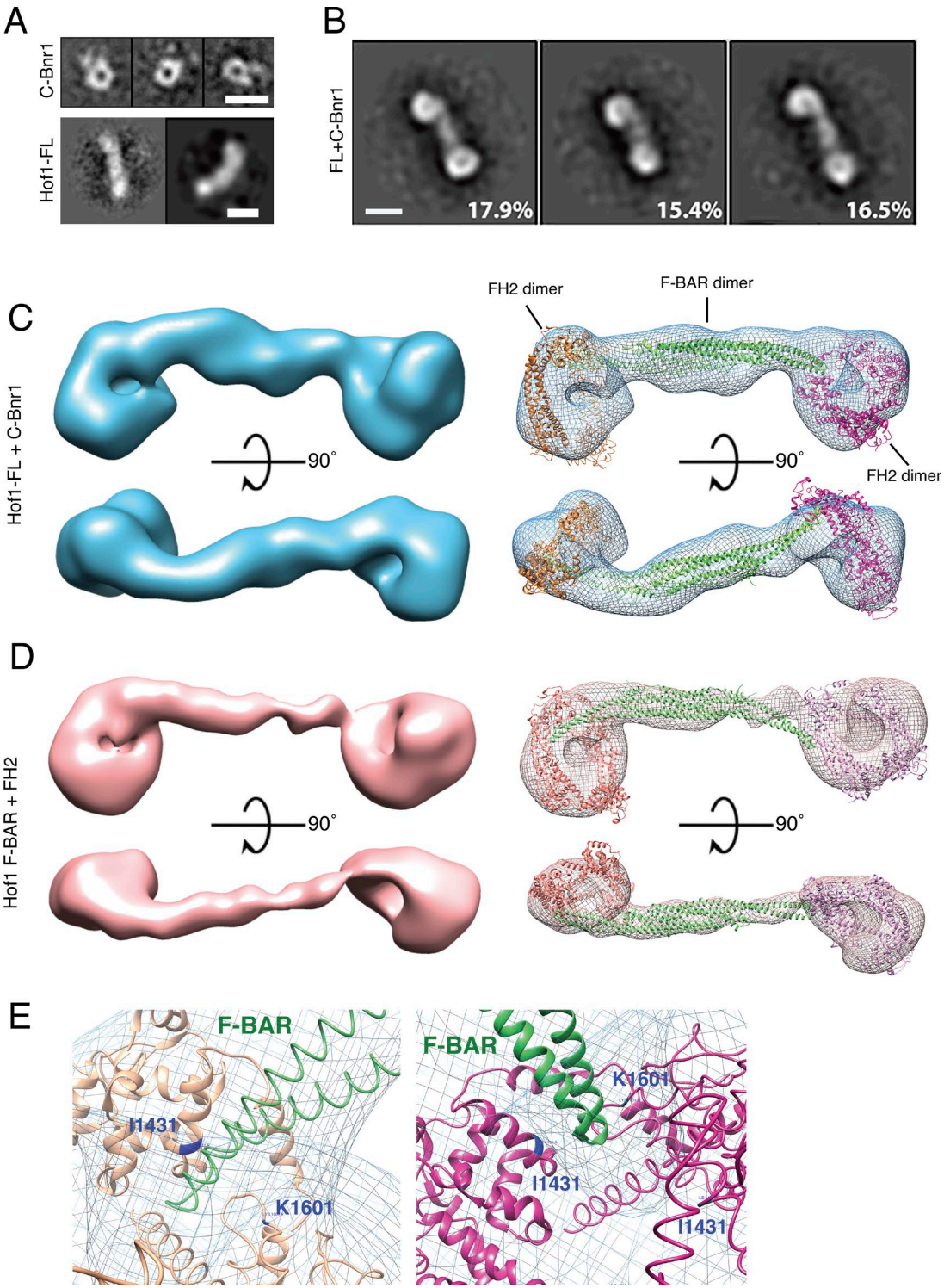

Figure 2. **EM structures of Hof1–Bnr1 complexes. (A)** Representative 2D class averages of C-Bnr1 alone and Hof1-FL alone. Bars, 10 nm. **(B)** Most abundant 2D class averages of complexes formed by C-Bnr1 + Hof1-FL (percentage of total particles that produced 2D average displayed). Bar, 10 nm. **(C)** 3D reconstruction of Hof1-FL bound to C-Bnr1 at 10 Å resolution. Crystal structures of Hof1 F-BAR domain and Bni1 FH2 domains docked into the EM density using UCSF Chimera. Note that we used the crystal structure of the Bni1 FH2 domain, because no structure is available for Bnr1 FH2. **(D)** 3D reconstruction of Hof1 F-BAR bound to Bnr1 (FH2) at 24-Å resolution, with crystal structures docked as above. **(E)** Close-up views of the Hof1-FL + C-Bnr1 structure, showing approximate positions of contact between the Hof1 F-BAR domain (green) and each of the two FH2 domains it binds, color-coded in gold and purple as in C. The tips of the F-BAR domains sit close to key actin-binding residues in the FH2 domain (K1601 and I1431).

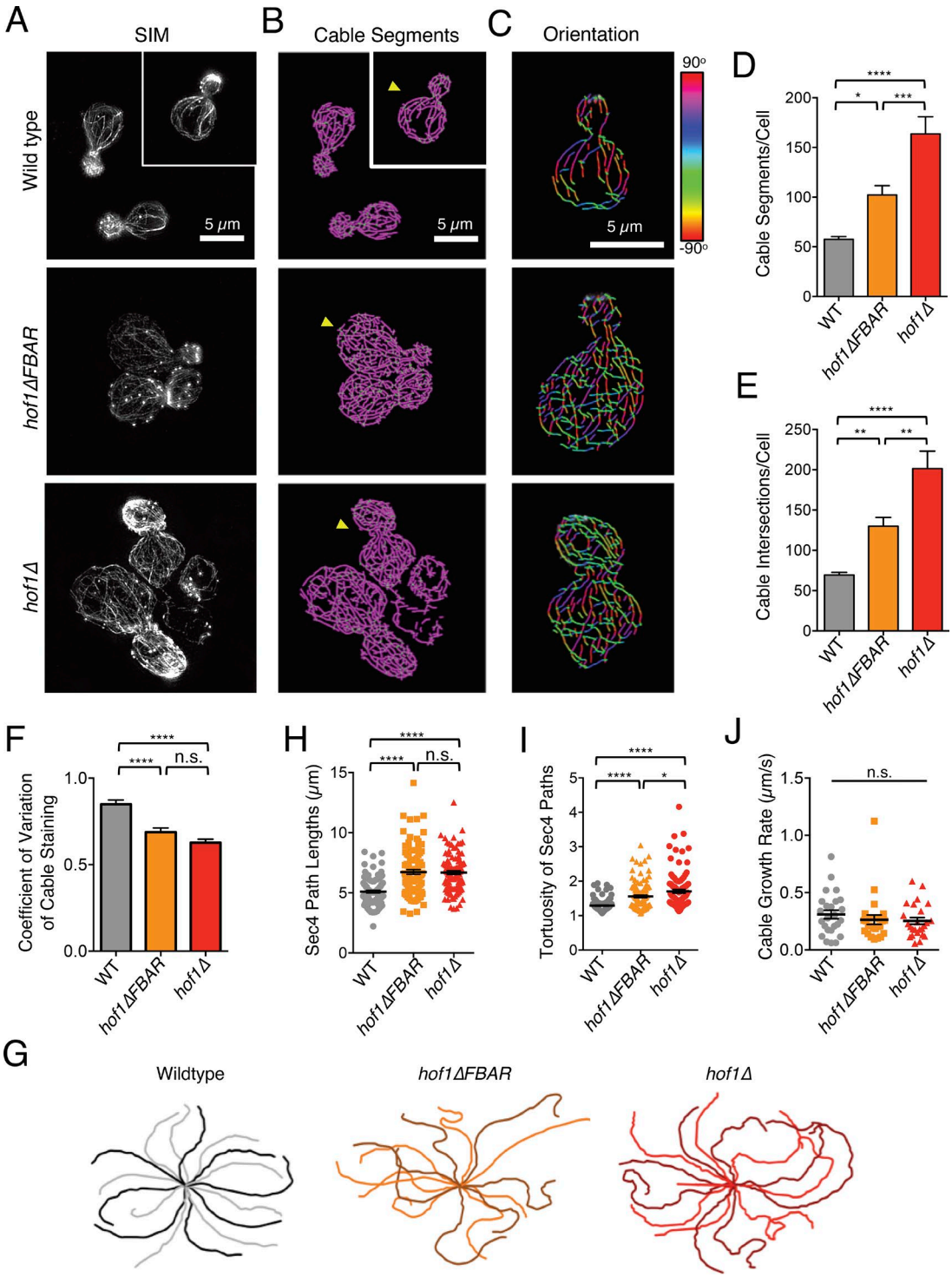

Figure 3. **Deletion of the Hof1 F-BAR domain in vivo gives rise to actin cable defects. (A)** SIM of F-actin organization in fixed wild-type, *hof1Δ,* and *hof1ΔFBAR* cells. **(B)** Automated analysis of actin cable organization from SIM images as in A with SOAX, showing cable segments (purple) and cable intersections (green). **(C)** Polarity map of actin cable segments in representative cells from the SIM images, with color-coding according to azimuthal orientation of cable segments relative to mother-bud axis. Azimuthal angle is defined such that the angle is zero when a cable segment is parallel with the x axis with a range of ±90 degrees. Cells analyzed marked with a yellow arrowhead in B. **(D)** Average number of cable segments per cell analyzed by SOAX, quantified for 20 cells per strain. **(E)** The same cells were quantified for number of cable intersections per cell by SOAX. **(F)** CVs of F-actin staining in mother cells after treatment with 100 μM CK666. Data were averaged for 20 cells in each strain. **(G)** Representative traces (18 for each strain) of GFP-Sec4 paths, tracking vesicle movement from its starting position in the mother cell until it reached the bud neck. Convergence point of traces indicates the bud neck. **(H)** Quantification of path lengths of GPF-Sec4 vesicle movements, imaged as above (n = 100 vesicles per strain). **(I)** Tortuosity (length/distance) of the paths of the same vesicles. **(J)** Quantification of actin cable extension velocities from live-imaging experiments using Abp140-3xGFP to decorate cables (n = 25 cables per strain). Error bars in all panels represent SEM. Statistical significance in all panels was calculated by one-way ANOVA (n.s., not significant; *, P ≤ 0.05; **, P ≤ 0.01; ***, P ≤ 0.001; ****, P ≤ 0.0001).

and more circuitous (Fig. 3 I) in *hof1ΔFBAR* and *hof1Δ* cells than in wild-type cells, consistent with disorganized cable networks. However, we note that Sec4-GFP paths are not necessarily a measure of cable length, since disorganized cables cross paths and vesicles may jump tracks during transport. Thus, while our data indicate that *hof1Δ* disrupts cable organization, it is unclear whether *hof1Δ* affects cable length.

We also used live-cell imaging to determine whether *hof1ΔFBAR* and *hof1Δ* mutations affect cable growth rates. Previously, we showed that *smy1Δ* causes abnormally fast cable growth rates in vivo, consistent with Smy1's inhibitory effects on Bnr1-mediated filament elongation (Chesarone-Cataldo et al., 2011; Eskin et al., 2016). Here, we found that cable growth rates were not significantly different in *hof1ΔFBAR* and *hof1Δ* cells compared with wild-type cells (Fig. 3 J), consistent with our biochemical data showing that Hof1 inhibits Bnr1-mediated nucleation and not elongation of actin filaments. These data also suggest that the defects in secretory traffic in *hof1ΔFBAR* and *hof1Δ* mutants are the result of defective cable organization rather than altered cable dynamics. Note that previously, we showed that *bnr1Δ* at least partially suppresses the cable defects of *hof1Δ* (Graziano et al., 2014). Here, we found that *bnr1Δ* fails to suppress the temperature-sensitive growth defects of *hof1Δ* (Fig. S3 D), suggesting that the temperature-sensitive growth defects of the *hof1Δ* strain arise at least in part from the loss of a different, Bnr1-independent function of Hof1.

Hof1 inhibition of Bnr1 is overcome by Bud6 in vitro

Our observations above raise an important question: how is the potent inhibition by Hof1 overcome in vivo to allow Bnr1-mediated actin assembly? We considered whether other ligands of Bnr1 may play a role, and based on available genetic and biochemical data, Bud6 was the best candidate. Deletion of *BUD6* dramatically reduces cable levels in vivo (Amberg et al., 1997), and purified Bud6 serves as a nucleation-promoting factor for Bni1 and Bnr1 in vitro, enhancing nucleation (Moseley and Goode, 2005; Graziano et al., 2011, 2013; Tu et al., 2012; Park et al., 2015). Moreover, point mutations in Bud6 that disrupt its interactions with formins (e.g., *bud6-35*; Fig. 4 A) and G-actin (e.g., *bud6-8*; Fig. 4 A) each abolish its nucleation-promoting factor effects in vitro and result in cable defects similar to *bud6Δ* mutants in vivo (Graziano et al., 2011; Tu et al., 2012).

To investigate the possible involvement of Bud6 in overcoming Bnr1 inhibition by Hof1, we tested the effects of purified C-Bud6 (550–788) on C-Bnr1 in the presence of Hof1-FL in TIRF assays. C-Bud6 enhanced C-Bnr1-mediated actin nucleation (Fig. S4 A), as reported previously (Graziano et al., 2011). The actin nucleation activity of C-Bnr1 was suppressed by Hof1-FL; however, addition of C-Bud6 strongly alleviated inhibition by Hof1-FL, triggering C-Bnr1–mediated actin assembly (Fig. 4, B and C). To gain additional insights into this mechanism, we tested C-Bud6-35 and C-Bud6-8 polypeptides. C-Bud6-35 failed to reverse Hof1 inhibition, demonstrating that binding to Bnr1 is required for Bud6 to overcome Hof1 inhibition. More unexpectedly, C-Bud6-8 was also defective in overcoming Hof1 inhibition, albeit less so than C-Bud6-35. Control TIRF reactions showed that C-Bud6-8 had no adverse effects on C-Bnr1–mediated actin nucleation alone (Fig. S4 A). Thus, Bud6 binding to G-actin is also important for overcoming Hof1 inhibition, although it is less crucial than Bud6 binding to Bnr1. In addition, we asked whether C-Bud6 is capable of overcoming Bnr1 inhibition by each half of Hof1: Hof1-NT and Hof1-CT (Fig. S4 B). This revealed that C-Bud6 overcomes Bnr1 inhibition by Hof1-NT, but not Hof1-CT. Since C-Bud6 overcomes Hof1-FL, which encompasses Hof1-CT, these observations have important implications for the regulatory mechanism (see Discussion).

Finally, we asked whether C-Bud6 competes with Hof1-NT for binding to C-Bnr1. To address this, we performed a quantitative visual assay, monitoring levels of soluble labeled Hof1-NT-SNAP-549 bound to immobilized 649-biotin-SNAP-C-Bnr1 on beads, in the presence and absence of unlabeled C-Bud6 (Fig. 4, D and E). Our results show that C-Bud6 decreases binding of Hof1-NT to Bnr1, indicative of competitive binding.

Genetic support for Bud6 releasing Hof1 inhibition of Bnr1 in vivo

Our biochemical data suggest that *BUD6* and *HOF1* have antagonistic roles in controlling Bnr1-mediated actin assembly. To test this model in vivo, we asked whether *bud6Δ* can suppress cell growth or actin cable defects of *hof1Δ* cells. Our results show that *bud6Δ* partially suppresses the cell growth defects of *hof1Δ* cells on plates and in liquid cultures (Fig. 5, A and B). Further, a comparison of F-actin organization by SIM revealed that *bud6Δ* suppresses the cable defects of *hof1Δ* (Fig. 5, C–E). Further, we treated these strains with CK666 to remove actin patches and improve the view of cable organization (Fig. 5 C, lower panels), and CV measurements in mother cells (described in Fig. 1) confirmed that *bud6Δ* suppresses the dispersed cable phenotype of *hof1Δ* (Fig. 5 F). Additionally, we used live-cell imaging to monitor secretory vesicle movements, as in Fig. 3, and found that *bud6Δ* suppressed the increased tortuosity of vesicle paths in *hof1Δ* mutants (Fig. 5 G). Live imaging of actin cable dynamics revealed no significant difference in cable extension velocities among wild-type, *hof1Δ*, *bud6Δ*, and *hof1Δbud6Δ* strains (Fig. S5 A). Thus, the cable phenotypes in these mutants likely arise from defects in actin nucleation rather than elongation, as suggested by our biochemical results.

We also asked whether cable defects in *hof1Δ* and suppression by *bud6Δ* occur at specific stages of bud development by comparing cable levels and organization in wild-type and mutant strains as a function of bud size (Fig. S5, B and C). Our results show that *hof1Δ* causes cable overgrowth and disorganization (with *bud6Δ* largely suppressing these defects) at medium- and large-budded stages, but not earlier in bud development. Collectively, these results support a model in which Hof1 plays an inhibitory role and Bud6 a stimulatory role in controlling Bnr1-mediated cable assembly during later stages of bud growth.

Bud6 localizes to secretory vesicles and is trafficked on cables to the bud neck

To better understand how Bud6 activates Bnr1-mediated cable assembly in vivo, we asked where Bud6 localizes in cells. Bnr1 and Hof1 both stably associate with septins at the bud neck, in a position to interact with each other throughout polarized growth

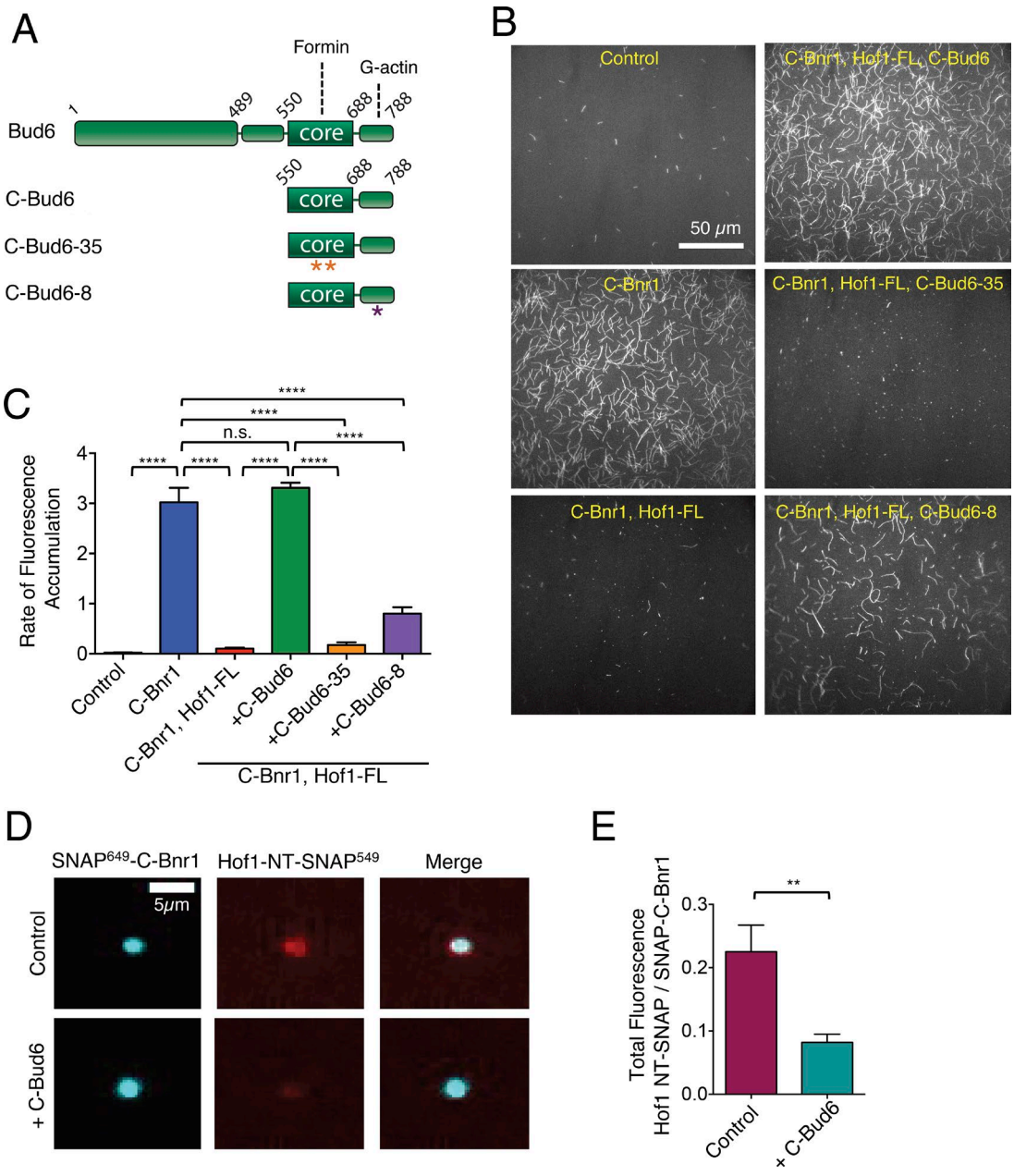

Figure 4. **Bud6 overcomes Hof1 inhibition of Bnr1-mediated actin assembly in vitro. (A)** Schematic of Bud6 domains and C-Bud6 polypeptides (wild type and mutant) used for in vitro assays. **(B)** Representative images from TIRF microscopy assays showing the effects of wild-type C-Bud6 and mutant C-Bud6-35 and C-Bud6-8 polypeptides on actin assembly in the presence of C-Bnr1 and Hof1-FL. All reactions contain 0.5 µM monomeric actin (10% OG labeled; 0.5% biotin-actin) and 3 µM yeast profilin and as indicated 0.2 nM C-Bnr1 (FH1-FH2-C), 20 nM Hof1-FL, and/or 100 nM C-Bud6 polypeptides. Images show representative FOVs 600 s after initiation of actin assembly. **(C)** Quantification of actin assembly rates from TIRF assays as in B. Rates of OG-labeled F-actin accumulation averaged from four FOVs in each of two independent experiments (eight FOVs total). Error bars represent SEM. Statistical significance was calculated by one-way ANOVA (n.s., not significant; ****, $P \le 0.0001$). **(D)** Representative TIRF images from binding assays. 500 nM soluble MBP-Hof1-NT-SNAP-549 incubated with beads coated with immobilized 649-biotin-SNAP-C-Bnr1 in the presence and absence of 200 nM unlabeled C-Bud6. Bar, 5 µm. **(E)** Quantification of MBP-Hof1-NT-SNAP-549 binding to beads, from assays as in D. Data were averaged from a total of 31 and 42 beads (±C-Bud6, respectively), imaged in three FOVs of two independent trials (six FOVs total for each). For each bead, the fluorescence of MBP-Hof1-NT-SNAP-549 was divided by the fluorescence of 649-biotin-SNAP-C-Bnr1 to control for variable levels of formin on the beads. Error bars represent SEM. Statistical significance was calculated by unpaired *t* test (**, $P \le 0.01$).

(Gao et al., 2010; Oh et al., 2013). Conversely, Bud6 localization has been more elusive. Bud6 was previously localized to puncta in the cytosol and to the bud neck and bud cortex (Amberg et al., 1997; Evangelista et al., 1997; Jin and Amberg, 2000; Segal et al., 2000; Delgehyr et al., 2008). The accumulation of Bud6 at polarity sites (bud neck and cortex) depends on myosin V (Myo2), and biochemical fractionation experiments have suggested that Bud6 may reside in a compartment of the secretory pathway (Jin and Amberg, 2000). However, the specific compartment has never been confirmed by microscopy. To address this, we integrated an mCherry tag at the C-terminus of Bud6 in yeast strains also carrying GFP tags on markers for different compartments: mito-

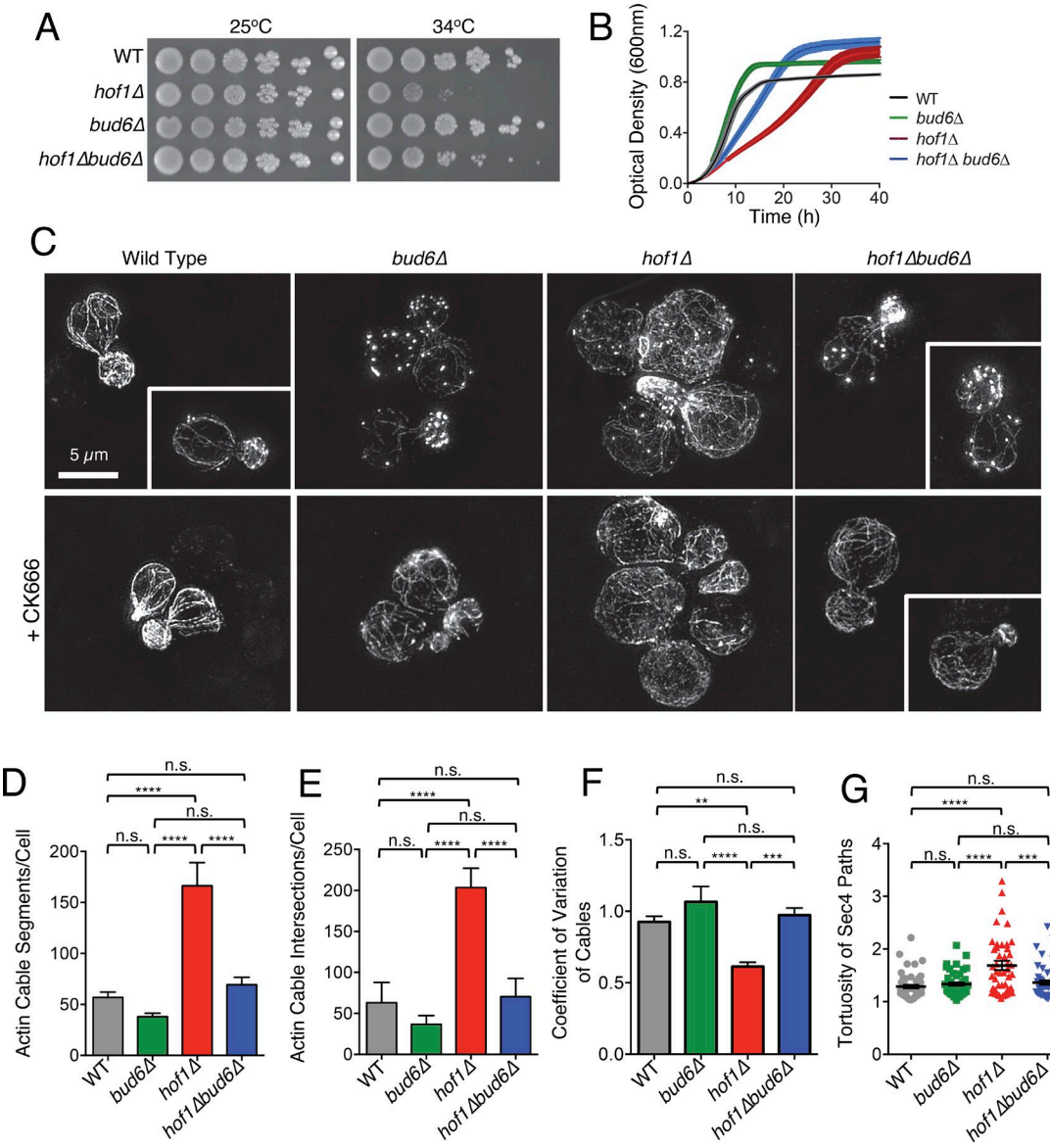

Figure 5. **Deletion of *BUD6* suppresses *hof1Δ* defects. (A)** Yeast strains (fivefold serial dilutions) grown at 25°C or 34°C on YEPD plates for 2 d. **(B)** Growth rates of the same strains measured by optical density (OD_{600}) at 34°C in liquid culture (YEPD) in a shaking microplate absorbance reader. Data were averaged from eight independent trials. Lighter shading represents SEM. **(C)** F-actin organization in the same strains imaged by SIM before and after treating cells with the Arp2/3 complex inhibitor CK666 to remove actin patches. **(D)** Number of actin cable segments per cell determined by SOAX analysis, averaged from 10 cells per strain. **(E)** Number of cable intersections determined by SOAX analysis for same cells as above. **(F)** CV analysis on cable fluorescence after treatment with CK666, analyzed for 20 mother cells per strain. **(G)** Tortuosity of GFP-Sec4 secretory vesicle paths (n = 50 vesicles per strain). Error bars represent SEM. Statistical significance in all panels calculated by one-way ANOVA (n.s., not significant; **, P ≤ 0.01; ***, P ≤ 0.001; ****, P ≤ 0.0001).

chondria, ER, cis-Golgi, trans-Golgi, and secretory vesicles (Figs. 6 A and S5 D). Pearson's colocalization analysis revealed strong colocalization of Bud6-mCherry with secretory vesicles, but not other compartments (Fig. 6 B). This was also evident by line-scan analysis (yellow arrows, Fig. 6, A and C), and live imaging showed that Bud6-mCherry spots moved together with GFP-Sec4 in the cytosol (Fig. 6, D and E). Thus, Bud6 resides on secretory vesicles.

We also quantified Bud6-mCherry levels in cells at different stages of bud growth and found that they remain fairly constant (Fig. 6 F). Similarly, Bnr1-GFP levels at the neck remained steady throughout bud growth. In contrast, Hof1-GFP levels at the neck were very low at unbudded and small-budded stages and steadily climbed during medium and large-budded stages (Fig. 6, G and H). This suggests that while Bnr1 and Bud6 are likely to function together in promoting actin nucleation at all stages of bud growth, the Hof1–Bud6 inhibition-and-relief mechanism may be engaged mainly during medium- and large-budded stages.

As mentioned earlier, secretory vesicles are transported along cables to the bud neck, where they pause for 1–3 s before moving into the bud. Therefore, our working model is that vesicles loaded with Bud6 pause and interact with Bnr1 at the neck, overcoming Hof1 inhibition to induce cable formation. This in turn stimulates more vesicle traffic, establishing a positive feedback loop in which Bud6 delivery stimulates assembly of the very cable

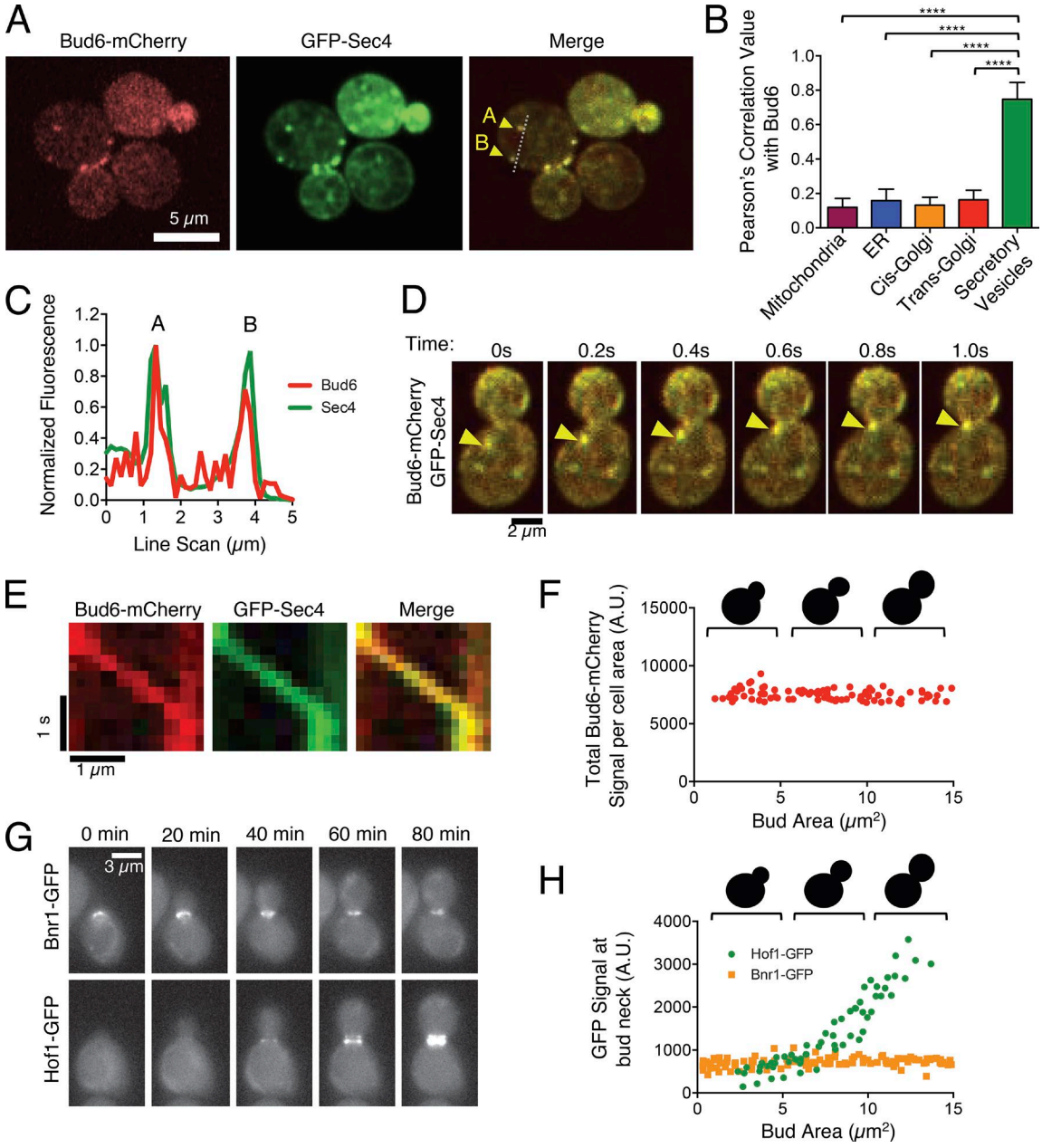

Figure 6. **Bud6 localizes to secretory vesicles and is transported on actin cables to the bud neck. (A)** Colocalization of Bud6-mCherry and GFP-Sec4 in live yeast cells. Bar, 5 µm. Merge highlights two puncta used in line scan analysis below. **(B)** Pearson's correlation analysis of Bud6-mCherry signal with GFP in strains containing GFP tags on different membrane compartments (n = 50 cells per strain). Error bars represent SEM. Statistical significance calculated by one-way ANOVA (****, P ≤ 0.0001). **(C)** Line-scan analysis shows overlap between Bud6-mCherry and GFP-Sec4 puncta, corresponding to puncta highlighted in A. **(D)** Time-lapse dual-color live imaging of Bud6-mCherry and GFP-Sec4. Arrow highlights the movement of a vesicle. **(E)** Kymograph showing Bud6-mCherry and GFP-Sec4 comigration. **(F)** Total Bud6-mCherry fluorescence level in cells of variable bud size from an asynchronous population (n = 100 cells). **(G)** Representative time-lapse images of Bnr1-GFP and Hof1-GFP strains after α-factor arrest/release. Bar, 3 µm. **(H)** Quantification of Bnr1-GFP and Hof1-GFP levels at the bud neck for each strain, from time lapse imaging in G (n = 5 cells per strain).

network on which it is transported (Fig. 7 A). As a final test of our model, we asked how shutting off secretory vesicle transport using a *myo2-66* temperature-sensitive allele (Johnston et al., 1991; Liu and Bretscher, 1992) affects actin cable levels. At the nonpermissive temperature (35°C), *myo2-66* mutants showed significantly decreased cable staining compared with wild-type cells (Fig. 7, B and C), similar to *bud6Δ* cells, which lends support to our model.

Discussion

In this study, we set out to understand how cells integrate multiple regulatory inputs to control formin-mediated actin assembly. We used *S. cerevisiae* as a model to study this problem, where actin cables assembled by formins grow rapidly, and yet their length and organization are tightly controlled to prevent overgrowth and misdirected vesicle traffic. By combining genetics, high-resolution in vivo imaging, TIRF microscopy, and structural

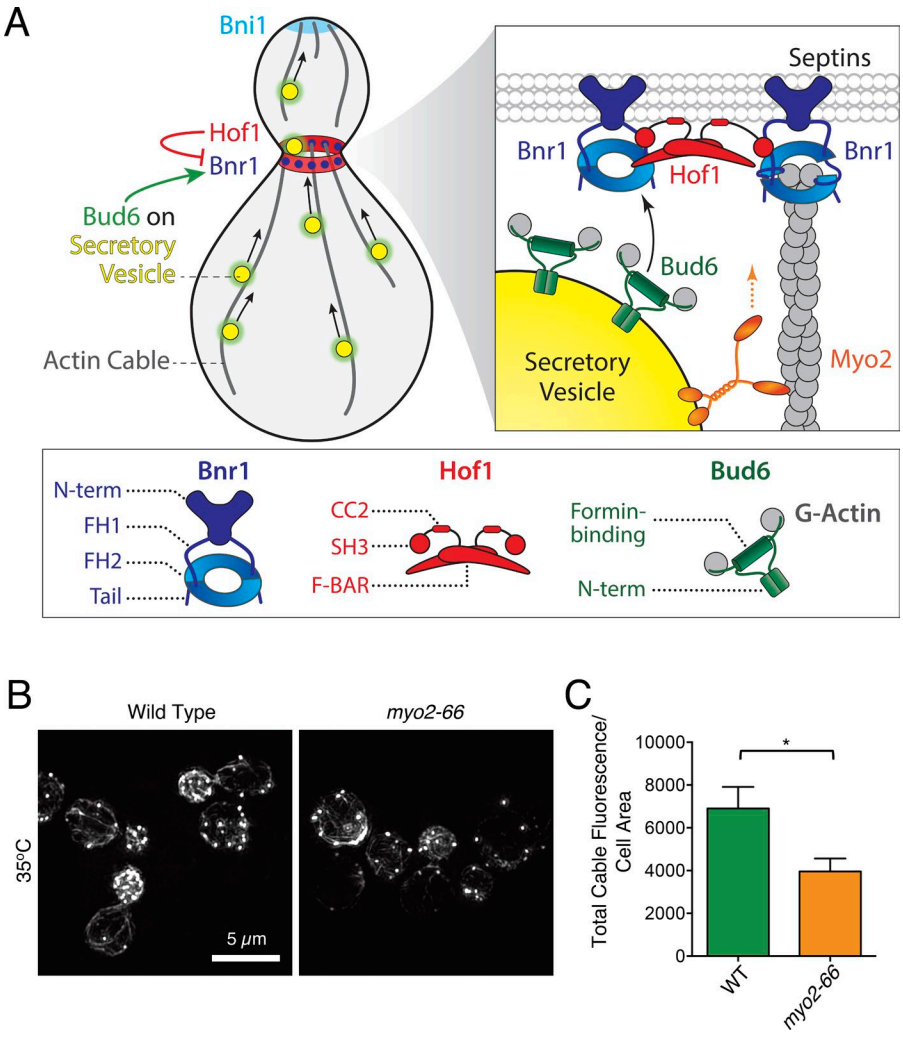

Figure 7. **Working model for Hof1-Bud6 positive feedback loop controlling Bnr1-mediated actin cable nucleation. (A)** Model showing myosin-mediated transport of secretory vesicles carrying Bud6 on actin cables to the bud neck, where Bnr1 and Hof1 reside. Close up on the right shows proposed interplay among Hof1, Bnr1, and Bud6 at the bud neck. **(B)** Representative SIM images of actin cable staining in wild-type and *myo2-66* cells 5 min after shift to 35°C. **(C)** Quantification of actin cable fluorescence levels in mother cells, from experiments as in B, averaged from 10 cells per strain. Error bars represent SEM. Statistical significance was calculated by unpaired *t* test (*, $P \le 0.05$).

EM, we uncovered a novel two-component integrated mechanism for controlling Bnr1-mediated actin assembly. Specifically, this mechanism consists of a high-affinity stationary inhibitor (Hof1) colocalized with Bnr1 at the neck and a mobile activator (Bud6) delivered by myosin V (Myo2) on actin cables. Purified Hof1-FL was found to be a highly potent inhibitor of Bnr1-mediated actin nucleation in vitro (K_{app} ~1.4 nM). Further, we solved the structure of the Hof1–Bnr1 complex at 10 Å resolution, revealing an intriguing molecular architecture, in which the tips of an elongated Hof1 F-BAR dimer hold apart two Bnr1 FH2 domains and appear to obstruct the actin-binding surfaces of the FH2. Combined with our previous work, these observations indicate that the potent inhibitory effects of Hof1-FL are derived from a combination of its F-BAR domain interacting with the FH2 domain of Bnr1 and its C-terminal SH3 domains interacting with the FH1 domains (Graziano et al., 2014).

Remarkably, Hof1 inhibition could be strongly reversed by Bud6 in vitro, and this required Bud6 interactions with Bnr1. The Bud6-binding site on formins is in the C-terminal tail extending from the FH2 domain (Moseley and Goode, 2005). Thus, Bud6 binding to the formin tail region relieves inhibition at the adjacent FH2 domain. Although the structural basis for the "release" is not yet clear, Bud6 competitively displaced the F-BAR–containing NT of Hof1 (Hof1-NT) from Bnr1. Interestingly, Bud6 could largely overcome inhibition of Bnr1 by Hof1-FL or by Hof1-NT, but not by the C-terminal SH3 domain–containing half of Hof1 (Hof1-CT). This raises an intriguing possibility, which is that after release from the formin FH2 domain, the F-BAR domain of Hof1 may in turn inactivate the SH3 domain of Hof1. Although this model requires further investigation, it is consistent with previous studies reporting autoinhibitory interactions between the F-BAR and SH3 domains of other F-BAR proteins (e.g., Syndapin, IRSp53, and Nervous Wreck; Rao et al., 2010; Kast et al., 2014; Kelley et al., 2015; Stanishneva-Konovalova et al., 2016).

In vivo, we found that Bud6 is on secretory vesicles, which are transported along cables to the bud neck; thus, Bud6 is a mobile activator of Bnr1-mediated actin nucleation. We propose that this establishes a positive feedback loop, in which successful delivery of Bud6 to the neck reinforces Bnr1-mediated cable assembly by overcoming Hof1 inhibition, which in turn promotes more Bud6 delivery (Fig. 7 A). Interestingly, we found that Bud6 binding to G-actin is also important for alleviating formin inhibition by Hof1. This suggests that the Bud6 activation mechanism may be sensitive to actin monomer levels in cells, pointing to another possible layer of feedback regulation. Importantly, loss of Bud6 function in vivo does not completely shut off Bnr1-dependent

cable assembly, but instead diminishes cable levels. It is not currently understood why the loss of cables in *bud6Δ* mutants is not more complete. However, one possibility is that Hof1 does not inhibit all of the Bnr1 at the neck, and another is that there are additional stimulatory inputs on Bnr1, besides Bud6, that help overcome Hof1 inhibition. It will be interesting to learn whether other components of the secretory vesicle itself contribute to Bnr1 activation, including the lipid membrane, since Hof1 is a lipid-binding F-BAR protein. Most F-BAR domains form crescent-shaped dimers, in which residues located on the concave surface bind to membranes (Hurley, 2006). Our EM structures show that the Bnr1 FH2 dimers dock at either tip of the elongated F-BAR dimer of Hof1, where FH2 binding may not interfere with membrane binding. Thus, it will be important to determine if and how Hof1 coordinates membrane and formin binding to govern cable assembly.

Functional roles of the F-BAR domain of Hof1

Our results support an emerging view that F-BAR domains can have diverse functions in governing the actin cytoskeleton. As mentioned earlier, F-BARs are best known for binding membranes and sensing or stabilizing curvature, but they also interact with other cellular factors to expand their mechanistic capabilities. Our results show that the F-BAR domain of Hof1 directly inhibits the FH2 domain of Bnr1 to control actin assembly in vitro and in vivo. In *Schizosaccharomyces pombe*, the F-BAR protein Cdc15 plays a crucial role in recruiting the formin Cdc12 to the division plane to promote cytokinesis (Carnahan and Gould, 2003; Willet et al., 2015, 2018). In contrast to Hof1, the F-BAR domain of Cdc15 binds to its formin target via a sequence located at the NT of the formin rather than the FH2 domain (Carnahan and Gould, 2003; Willet et al., 2015, 2018). We were unable to identify a similar F-BAR–binding motif in Bnr1 or Bni1, consistent with there being key differences in the functions of Hof1 and Cdc15, as previously noted (McDonald et al., 2016). Nonetheless, these observations leave open the possibility that Imp2, another important F-BAR domain protein at the division plane in *S. pombe*, uses its F-BAR and/or SH3 domains to control Cdc12 activity (McDonald et al., 2016). Still another F-BAR protein that may use a Hof1-like mechanism to control formins is CIP4/Toca-1, which in developing *Drosophila melanogaster* interacts with the formins DIA and DAAM to promote membrane extension and cellularization (Aspenström et al., 2006; Yan et al., 2013). Like Hof1, CIP4 has been shown to inhibit DIA-mediated actin assembly through an interaction of its C-terminal SH3 domain with the FH1 domain (Yan et al., 2013). Our results raise the possibility that CIP4/Toca-1 also uses its F-BAR domain to inhibit the FH2 domain of DIA and, consistent with this view, constructs lacking the F-BAR showed diminished inhibitory effects on DIA in the aforementioned study.

Implications for actin regulation in other systems

Our results also broaden our understanding of the mechanisms by which formins can be regulated in vivo, demonstrating for the first time that a formin can be held inactive by one binding partner at a fixed location until the arrival of a second binding partner that alleviates inhibition and triggers actin assembly (Fig. 7 A). This novel paradigm for formin regulation is predicted to provide exceptionally tight spatial and temporal control over actin assembly. It also begins to explain how inputs from multiple formin regulators are integrated to control actin assembly. Related mechanisms may be used in other biological settings. For example, the tumor suppressor protein APC, which collaborates with Dia and Daam1 (and possibly other formins) to promote actin nucleation (Okada et al., 2010; Breitsprecher et al., 2012; Juanes et al., 2017) is transported by kinesins along microtubules, accumulating at their plus ends, and then deposited at actin-rich cortical sites in cells (Mimori-Kiyosue et al., 2000; Jimbo et al., 2002; Kita et al., 2006; Ruane et al., 2016). The arrival of APC at cortical sites may trigger collaborative actin assembly with formins, in a manner related to Bud6 arrival at the bud neck triggering cable assembly. In the case of APC-Dia, actin assembly is hypothesized to promote further capture of microtubule plus ends at the leading edge (Zaoui et al., 2010), and therefore may establish a positive feedback loop between microtubules and actin. APC and Bud6 may be functional homologues, as they both bind actin and formins, mediate collaborative actin nucleation, bind to the microtubule end–binding protein EB1, and facilitate microtubule plus-end capture at cortical sites in vivo (Segal et al., 2002; Huisman et al., 2004; Zaoui et al., 2010; Ten Hoopen et al., 2012). Interestingly, Bud6 appears to behave more like APC in *S. pombe*, where it is delivered on microtubules by kinesin to the cell cortex, where it promotes formin-mediated actin assembly (Martin et al., 2007). These mechanistic differences may reflect the different roles microtubules and actin play in directing intracellular transport in symmetrically and asymmetrically dividing cells. Both the mammalian and yeast systems provide fertile ground for future studies aimed at dissecting microtubule–actin crosstalk and feedback regulation of formins involving APC and/or Bud6.

Materials and methods

Plasmids and yeast strains

Standard methods were used for general molecular biology and *S. cerevisiae* work (Sambrook et al., 1989; Guthrie and Fink, 1991). Low-copy (CEN) plasmids for expressing *GFP-SEC4* and *COX4-GFP* in *S. cerevisiae* and integrating *ABP140-3xGFP::LEU2* have been described (Calero et al., 2003; Buttery et al., 2007). Plasmids for galactose-inducible expression in *S. cerevisiae* of 6His-fusions of Bnr1 FH1-FH2-C (residues 757–1,375) and Bnr1 FH2 (868–1,291) have been described previously (Moseley and Goode, 2005; Okada et al., 2010; Jaiswal et al., 2013). Plasmids used for *Escherichia coli* expression of MBP-Hof1 NT (1–340), MBP-Hof1 F-BAR (1–275), and MBP-Hof1 CC2 (276–340) were gifts from E. Bi (University of Pennsylvania, Philadelphia, PA) and have been described elsewhere (Oh et al., 2013). To construct a plasmid for expressing Hof1-FL that has an N-terminal MBP tag and a C-terminal 6His tag, the *HOF1* ORF was PCR amplified with the 6His tag encoded in the reverse primer (forward, 5′-ATCGCT GGATCCATGAGCTACAGTTATGAAGCTTG-3′; reverse, 5′-TTGTCA GTCGACTCAATTAGTGGTGGTGGTGGTGG-3′) and cloned into the BamHI and SalI sites of pMALc2. To generate a *hof1ΔFBAR-GFP::HIS3 (Δ2-275)* yeast strain (BGY3917), we used Cas9-mediated

gene editing as described (Anand et al., 2017). Complementary 20-nt DNA oligos (Integrated DNA Technologies) with homology to the Hof1 F-BAR sequence (forward, 5′-CAACAAGAAAAA GGGGTGTGGTTTT-3′; reverse, 5′-CACACCCCTTTTTCTTGT TGGATCA-3′) were designed with overhangs for BplI cut sites were duplexed by and cloned into the BplI restriction site of the bRA90 plasmid to be transcribed as the Cas9 gRNA. This plasmid was then transformed into a *HOF1*-GFP::*HIS3* strain, along with 80mer DNA oligos homologous to the 5′ UTR and sequences downstream of the F-BAR domain (5′-GAAAGTGTACTACTA ATATTCAGAAAAAGGTGAAAGAATGCATAAGACTTCCAAAGG TGACATGAATTCTAGCGCCAACT-3′), and grown on synthetic media lacking leucine to select for the Cas9 plasmid. Internal deletion of the F-BAR domain was confirmed by PCR. Strains used for colocalization experiments were generated by cross or transformation. *BUD6*-mCherry::*HIS3 SEC63*-GFP::*HIS3* strain (BGY3919) was generated by crossing *BUD6*-mCherry::*HIS3* (BGY3912) with *SEC63*-GFP::*HIS3* (BGY3914). *BUD6*-mCherry::*HIS3 RER1*-GFP::*HIS3* strain (BGY3921) was made by crossing BGY3912 with *RER1*-GFP::*HIS3* (BGY3915). A PCR fragment to C-terminally integrate GFP on *SEC7* was transformed into the *BUD6*-mCherry::*HIS3* strain (BGY3916). Bud6-mCherry::*HIS3* (BGY3913) was also was transformed with CEN plasmids to express *COX4*-GFP::*URA3* (pDO10) or GFP-*SEC4*::*URA3* (pRC2098). The *hof1Δ::HIS3 bud6Δ::KANMX6* yeast strain (BGY3922) was generated by crossing *hof1Δ::HIS3* (BGY1277) and *bud6Δ::KAN MX6* (BGY1279). *ABP140-3xGFP::LEU2* was integrated into the endogenous *ABP140* locus by cutting pB1994 with NdeI and standard transformation of yeast strains. HOF1-GFP::HIS3 (BGY1284) and BNR1-GFP::KAN (BGY1302) were generated by integration of a C-terminal GFP tag and auxotrophic marker (Longtine et al., 1998). All yeast strains used in this study are in the Research Genetics background (Mata, *ura3Δ0, leu2Δ0, his3Δ1, met15Δ0* or Matα, *ura3Δ0, leu2Δ0, his3Δ1, lys2Δ0*), with the exception of wild-type s288c (*lys2-801, his3Δ200, ura3-52, leu2-3, 112, trp1-1*) and myo2-66 mutant (JP7B; *ade1 his3-Δ1 leu2-3,112 trp1-289 ura3-52*; Johnston et al., 1991).

Protein purification

Rabbit muscle actin was purified as previously described (Spudich and Watt, 1971) from acetone powder made from frozen ground skeletal muscle of young rabbits (PelFreez). Lyophilized acetone powder stored at −80°C was mechanically sheered in a coffee grinder, resuspended in G-buffer (5 mM Tris-HCl, pH 7.5, 0.5 mM DTT, 0.2 mM ATP, and 0.1 mM $CaCl_2$). Actin was then cleared by centrifugation for 20 min at 50,000 × *g*. Actin was polymerized by addition of 2 mM $MgCl_2$ and 50 mM NaCl and incubated overnight at 4°C. F-Actin was pelleted by centrifugation for 150 min at 361,000 × *g*. The F-actin pellet was solubilized by Dounce homogenization and dialyzed against G-buffer for 48 h at 4°C to depolymerize the actin. The G-actin was then precleared at 435,000 × *g* and gel filtered on an S200 (16/60) column (GE Healthcare) equilibrated in G-buffer. Peak actin-containing fractions were stored at 4°C and used within 2 wk. To label actin with either Biotin or Oregon Green (OG) dye on cysteine 374, an F-actin pellet was dounced and dialyzed against G-buffer lacking DTT. Then the G-actin was polymerized by adding an equal volume of 2× labeling buffer (50 mM Imidazole, pH 7.5, 200 mM KCl, 0.3 mM ATP, and 4 mM $MgCl_2$). After 5-min incubation at 25°C, actin was mixed with a fivefold molar excess of either NHS-XX-Biotin (Merck KGaA) or OG-488 iodoacetamide (Invitrogen), resuspended in anhydrous dimethylformamide, and incubated in the dark for 15 h at 4°C. Labeled F-actin was pelleted as above, and the pellet was rinsed with G-buffer, depolymerized by Dounce homogenization, and dialyzed against G-buffer for 48 h at 4°C. Labeled, monomeric actin was then applied to an S200 (16/60) gel filtration column as above. For biotin-actin, peak fractions were aliquoted, snap frozen in liquid N_2, and stored at −80°C. For OG-actin, peak fractions were dialyzed for 15 h against G-buffer with 50% glycerol and stored at −20°C. To label actin with pyrenyl-iodoacetamide on cysteine 374 (Pollard and Cooper, 1984; Graziano et al., 2013), an F-actin pellet prepared as above was dialyzed against pyrene buffer (25 mM Tris-HCl, pH 7.5, 100 mM KCl, 0.3 mM ATP, and 2 mM $MgSO_4$) for 4 h and then diluted with pyrene buffer to 1 mg/ml (23.8 µM). A 10-fold molar excess of pyrenyl-iodoacetamide was added, and the actin solution was incubated overnight at 4°C. The reaction was then centrifuged for 3 h at 4°C at 40,000 rpm in a Ti60 rotor (Beckman Coulter) to pellet the F-actin. F-actin pellets were dounced and then dialyzed against G-buffer for 48 h to depolymerize the actin. The G-actin was fractionated on a S200 (16/60) column equilibrated in G-buffer, and peak fractions were pooled, aliquoted, snap frozen in liquid N_2, and stored at −80°C.

S. cerevisiae profilin (Pfy1) was expressed in BL21(DE3) *E. coli* and purified as described previously (Graziano et al., 2013). Bacterial cells were grown in terrific broth to log phase and induced with 0.4 mM IPTG for 3–4 h at 37°C. Cells were pelleted and stored at −80°C. Frozen pellets were thawed, resuspended in lysis buffer (20 mM Tris-HCl, pH 8.0) supplemented with a protease inhibitor cocktail (1 mM PMSF and 0.5 µM each of pepstatin A, antipain, leupeptin, aprotinin, and chymostatin), and lysed by incubation with lysozyme and sonication. Lysates were cleared by centrifugation at 80,000 rpm at 4°C for 20 min in a TLA-100.3 rotor (Beckman Coulter). The supernatant was then loaded on a 5 ml HiTrap Q fast flow column (GE Healthcare) and eluted with a 75 ml salt gradient (0–400 mM NaCl) in 20 mM Tris-HCl, pH 8.0. Peak fractions were pooled, concentrated to a total volume of 5 ml and then fractionated on a Superdex (26/60) gel filtration column (GE Healthcare) equilibrated in G-buffer. Peak fractions were pooled, aliquoted, snap frozen in liquid N_2, and stored at −80°C.

C-Bnr1, Bnr1 FH2 polypeptides were expressed as N-terminal 6His-fusions in *S. cerevisiae* strain BJ2168 from high-copy plasmids under the control of a galactose-inducible promoter (Moseley et al., 2006). For each purification, 2 liters of yeast cells were grown in synthetic medium lacking uracil with 2% raffinose to an OD_{600} of 0.6–0.9. Then, expression was induced by addition of dry ingredients (10 g yeast extract, 20 g peptone, and galactose; 2% wt/vol). Cells were grown for 12–16 h at 30°C and then pelleted, washed in H_2O, frozen in liquid N_2, and stored at −80°C. Yeast was lysed mechanically in a coffee grinder cooled with liquid N_2. Then, 20 g of lysed yeast powder was resuspended in 20 ml of buffer A (20 mM $NaPO_4$, pH 7.4, 150 mM NaCl, 30 mM imidazole, 0.5 mM DTT, and 1% NP-40) supplemented with prote-

ase inhibitor cocktail as above and cleared by ultracentrifugation at 80,000 rpm for 20 min in a TLA100.3 rotor. Cleared lysates were then passed through a 0.45-µm syringe filter (Millex; MilliporeSigma), and the 6His-tagged Bnr1 polypeptides were isolated using a Profinia purification system (Bio-Rad) on a nickel (IMAC) column with desalting program (1 ml IMAC column and 5 ml desalting column). The proteins, which elute from the desalting column in 4 ml of $HEKG_{10}D$ buffer (20 mM Hepes, pH 7.5, 1 mM EDTA, 50 mM KCl, 10% [vol/vol] glycerol, and 1 mM DTT), were concentrated to ∼200 µl and then aliquoted, snap frozen in liquid N_2, and stored at −80°C.

SNAP-C-Bnr1 (FH1-FH2-C) was expressed as an N-terminal 6His-fusion in *S. cerevisiae* strain BJ2168 from a high-copy plasmid under the control of a galactose-inducible promoter. Cells were galactose-induced and lysed in liquid N_2 as above. 10 g of frozen lysed yeast powder was resuspended in 10 ml of Buffer A supplemented with protease inhibitor cocktail as above, thawed, and cleared by ultracentrifugation at 80,000 rpm for 20 min at 4°C in a TLA100.3 rotor. Supernatants were harvested, passed through a 0.45-µm syringe filter, and then incubated with 0.5 ml Ni–NTA beads for 1 h at 4°C. Beads were washed five times with Buffer B (Buffer A lacking protease inhibitors and NP-40). SNAP-C-Bnr1 was labeled while still on the beads by incubation overnight at 4°C with a fivefold molar excess of BG-649-PEG-Biotin and then washed with Buffer B and eluted with Buffer B supplemented with 300 mM imidazole. Eluted SNAP-C-Bnr1 was purified further on a Superose 12 gel filtration column (GE Healthcare) equilibrated in $HEKG_{10}D$. Peak fractions were snap frozen in liquid N_2 and stored at −80°C.

MBP-Hof1 polypeptides (F-BAR, NT, and CC2) were expressed in BL21(DE3) *E. coli* cells carrying the pRARE plasmid (MilliporeSigma). Cells were grown to late log phase (OD_{600} of 0.7–0.9) in terrific broth supplemented with ampicillin and chloramphenicol to maintain selection of the expression plasmid and the pRARE plasmid, respectively. Expression was induced with 0.4 mM IPTG overnight at 18°C, and then cells were pelleted and stored at −80°C. Cell pellets were thawed, resuspended in lysis buffer (20 mM Tris-HCl, pH 8.0, and 400 mM NaCl) with the same protease inhibitor cocktail as above, and lysed by treatment with lysozyme and sonication. Lysates were cleared by centrifugation at 13,000 rpm for 20 min in an F21S-8×50y rotor (Thermo Fisher Scientific), and the supernatant was mixed with 0.5 ml of amylose beads (New England Biolabs) and rotated at 4°C for 1 h. The beads were then washed five times with 5 ml lysis buffer. Hof1 constructs were eluted with lysis buffer plus 20 mM maltose and 1 mM DTT. Finally, eluted protein was exchanged into $HEKG_{10}D$ using a PD10 desalting column (GE Life Sciences) and collected in 0.3-ml fractions. Peak fractions were aliquoted and snap frozen in liquid N_2 and stored at −80°C. MBP-Hof1-NT-SNAP was expressed and purified similarly, except that peak fractions eluted from the amylose beads were incubated with a fivefold molar excess of BG-549 SNAP dye overnight at 4°C. The protein was then exchanged into $HEKG_{10}D$ on a PD10 desalting column as above, collecting 0.3-ml fractions. Peak fractions were snap frozen in liquid N_2 and stored at −80°C.

MBP-Hof1-FL-6His was expressed, stored, lysed, and cleared as above, and then the supernatant was mixed with 0.5 ml Ni-NTA beads and incubated at 4°C for 1 h. The beads were then washed five times with 5 ml lysis buffer plus 50 mM imidazole. MBP-Hof1-FL-6His was eluted with lysis buffer plus 300 mM imidazole in 0.5-ml fractions. Eluted proteins were diluted fourfold with buffer lacking imidazole and then mixed with 0.5 ml amylose beads and incubated at 4°C for 1 h. The beads were washed five times with 5 ml lysis buffer, and then the Hof1 polypeptide was eluted with lysis buffer plus 20 mM maltose and 1 mM DTT. Finally, the eluted protein was exchanged into $HEKG_{10}D$ using a PD10 desalting column (GE Life Sciences) and collected in 0.3-ml fractions. Peak fractions were snap frozen in liquid N_2 and stored at −80°C. For EM experiments, all proteins were purified as above except the final desalting buffer was HEKD (20 mM Hepes, pH 7.5, 1 mM EDTA, 50 mM KCl, and 1 mM DTT) supplemented with 150 mM NaCl.

GST-Hof1-CT-6His was expressed in BL21(DE3) *E. coli* cells carrying the pRARE plasmid. Cells were grown to OD_{600} of 0.7–0.9 in terrific broth supplemented with kanamycin and chloramphenicol. Expression was induced and cells were pelleted, washed, lysed, and centrifuged as above for other Hof1 polypeptides. The supernatant was mixed with 0.5 ml Ni-NTA beads and incubated at 4°C for 1 h Beads were washed five times with 5 ml lysis buffer plus 50 mM imidazole, and then GST-Hof1-CT-6His was eluted using lysis buffer plus 300 mM imidazole, collecting 0.5-ml fractions. Peak fractions were pooled, diluted fourfold with buffer lacking imidazole, mixed with 0.5 ml glutathione agarose beads (Thermo Fisher Scientific), and incubated at 4°C for 1 h. Beads were washed five times with 5 ml lysis buffer, and then GST-Hof1-CT-6His was eluted using lysis buffer plus 30 mM glutathione and 1 mM DTT. The eluted protein was exchanged into $HEKG_{10}D$ buffer on a PD10 desalting column (GE Life Sciences), aliquoted, snap frozen in liquid N_2, and stored at −80°C.

GST-C-Bud6 (550–788) was expressed in BL21(DE3) cells and purified as described previously (Graziano et al., 2013). Cells were grown in terrific broth to late log phase, induced using 0.4 mM IPTG overnight at 18°C, and then pelleted and frozen at −80°C. Pellets were thawed, resuspended in lysis buffer (50 mM Tris, pH 8.5, 150 mM NaCl, 5 mM EDTA, 1.5% sarkosyl, and 5 mM DTT) supplemented with protease inhibitors as above, and lysed with lysozyme and sonication. Cell lysates were cleared by centrifugation at 13,000 rpm for 20 min in a Sorvall S600 rotor (Thermo Fisher Scientific). Triton X-100 (final concentration 3.3% [vol/vol]) was added to the supernatant, which then was mixed with 1 ml preswollen glutathione agarose in PBS (137 mM NaCl, 2.7 mM KCl, 4.3 mM Na_2HPO_4, and 1.47 mM KH_2PO_4, pH 7.4). After incubation at 4°C for 1 h, beads were washed four times with PBS and then twice with HEKD. C-Bud6 polypeptides were cleaved from GST by digestion with TEV protease for 2 h at room temperature, aliquoted, and snap frozen.

Bulk actin assembly assays

Kinetics of pyrene-actin assembly were measured as described (Graziano et al., 2014). Actin assembly reactions were performed in a final volume of 60 µl, using 2 µM G-actin (5% pyrene labeled). 38 µl of G-actin was converted to Mg^{2+}-ATP-actin ∼2 min at ambient temperature before use by mixing with 4 µl of exchange buffer (10 mM EDTA and 1 mM $MgCl_2$). Then, 15 µl of proteins

and/or control buffer ($HEKG_{10}$) was added, and finally 3 µl of 20× initiation mix (40 mM $MgCl_2$, 10 mM ATP, and 1 M KCl) was added to initiate actin polymerization. Fluorescence was monitored at excitation 365 nm and emission 407 nm in a spectrophotometer at ambient temperature (Photon Technology International). Rates of pyrene-actin assembly were determined from the slopes of the curves where they reached 50% maximum polymerization. To plot concentration-dependent activities of each Bnr1 polypeptide, the assembly rate of Bnr1 alone (without Hof1) was arbitrarily set to 1.0 (Fig. 1 D). The concentration of each Hof1 polypeptide required for half-maximal inhibition (K_{app}) of Bnr1 activity was determined by fitting a hyperbolic decay curve to the data in GraphPad Prism (GraphPad Software).

TIRF microscopy

For TIRF microscopy experiments, 24 × 60-mm coverslips (Thermo Fisher Scientific) were cleaned by sonication in detergent for 60 min and rinsed thoroughly in sterile water, followed by sonication in 1 M KOH for 20 min and 1 M HCl for 20 min and finally sonication in ethanol for 60 min. Coverslips were then washed extensively with sterile water, dried in an N_2 stream, and coated with 200 µl of 80% ethanol, pH 2.0, 2 mg/ml methoxy-poly(ethylene glycol)-silane, and 2 µg/ml biotin-poly(ethylene glycol)-silane (Laysan Bio Inc.). Coverslips were incubated at 70°C for 1–3 d before use. Flow cells were assembled just before imaging by rinsing coverslips extensively with sterile water, attaching coverslips to a plastic flow chamber (Ibidi) using double-sided tape 2.5 cm × 2 mm × 120 µm (Grace Bio-Labs), and sealing both ends with epoxy resin (Devcon).

Immediately before each experiment, flow cells were incubated for 30 s with HBSA (20 mM Hepes, pH 7.5, 1 mM EDTA, 50 mM KCl, and 1% BSA), incubated for 60 s in 0.1 mg/ml streptavidin in $HEKG_{10}$, and then washed with TIRF buffer (10 mM imidazole, 50 mM KCl, 1 mM $MgCl_2$, 1 mM EGTA, 0.2 mM ATP, 10 mM DTT, 15 mM glucose, 20 µg/ml glucose oxidase, and 0.5% methylcellulose [4,000 cP], pH 7.4). Proteins in TIRF buffer were mixed with 0.5 µM G-actin (10% OG labeled, 0.5% biotin labeled) and then flowed into the chamber. Images were acquired in ambient temperature at 10-s intervals for 600 s using an inverted Ti200 TIRF microscope (Nikon Instruments) equipped with 100-mW solid-state lasers (Agilent Technologies), a CFI Apo 60× TIRF objective (NA 1.49; Nikon Instruments), and an iXon EMCCD camera (Andor Technology). Focus was maintained using the Perfect Focus System (Nikon Instruments). The number of actin filaments in each field of view (FOV) was measured 600 s after initiation of assembly and the rate of fluorescence accumulation was measured from the slope of fluorescence over time using ImageJ.

TIRF microscopy was also used to directly visualize binding of labeled MBP-Hof1-NT-SNAP-549 to labeled 649-biotin-SNAP-C-Bnr1 immobilized on beads in the presence and absence of unlabeled C-Bud6 (Fig. 4, D and E). For these assays, 24 × 60-mm coverslips (Thermo Fisher Scientific) were cleaned as above and coated with 200 µl of 80% ethanol, pH 2.0, 4 mg/ml methoxy-poly(ethylene glycol)-silane, and 80 µg/ml biotin-poly(ethylene glycol)-silane (Laysan Bio Inc.). Coverslips were incubated at 70°C for 1–3 d before use. Flow cells were assembled as described for TIRF assays above. Immediately before imaging, 60 µg of 2 µm biotinylated polystyrene microspheres (Polysciences Inc.) were washed three times in Buffer A (10 mM imidazole, pH 7.5, 50 mM KCl, 1 mM $MgCl_2$, and 1 mM EGTA). The microspheres were then incubated in 600 µl of Buffer A with 4 µg/ml streptavidin (2.4 µg) and 300 ng of 649-biotin-SNAP-C-Bnr1 for 20 min on ice to allow formin binding to the beads. After this incubation period, the formin-coated beads were washed three times in Buffer A to remove any unbound formin and then resuspended in 50 µl of Buffer A. Immediately before each TIRF reaction, 5 µl of formin-coated beads was diluted 10-fold into Buffer A (50 µl total) and incubated for 10 min in a TIRF flow cell at ambient temperature to allow beads to settle. Then, 50 µl of HEK buffer supplemented with 1% BSA was flowed into the cell to block nonspecific binding sites, followed by HEK buffer and then TIRF buffer (10 mM imidazole, 50 mM KCl, 1 mM $MgCl_2$, 1 mM EGTA, 0.2 mM ATP, 10 mM DTT, 15 mM glucose, 20 µg/ml glucose oxidase, and 3% Dextran) containing 500 nM Hof1-NT-SNAP-549 with or without 200 nM C-Bud6. After a 10-min incubation period, images were captured at ambient temperature using an inverted Ti200 TIRF microscope equipped with 100-mW solid-state lasers (Agilent Technologies), a CFI Apo 60× TIRF objective, and an EMCCD camera (Andor Technology). Focus was maintained using the Perfect Focus System.

Live-cell imaging and analysis

For measuring in vivo actin cable elongation rates, yeast cells expressing Abp140-3xGFP from the endogenous locus were grown to mid-log phase (OD_{600} 0.4–0.6) in synthetic media. Live cells in media were mounted on slides with coverslips and immediately imaged at ambient temperature on an i-E upright confocal microscope (Nikon Instruments) equipped with a CSU-W1 spinning disk head (Yokogawa), 100× oil objective (NA 1.4; Nikon Instruments), and an Ixon 897 Ultra-CCD camera (Andor Technology) controlled by NIS-Elements software (Nikon Instruments). Actin cables were analyzed in a single optical plane, capturing images 120 s. Individual cells were cropped using ImageJ. Actin cable extension speeds were measured using custom software written in MATLAB (MathWorks; Eskin et al., 2016). For imaging secretory vesicle transport, wild-type and mutant yeast strains were transformed with a CEN plasmid expressing GFP-Sec4 (Calero et al., 2003). Cells were grown to mid-log phase (OD_{600} 0.4–0.6) in synthetic selective media, then mounted on a microscope slide and imaged at ambient temperature on an inverted Ti200 microscope equipped with an Intensilight excitation source (Nikon Instruments), 100× objective (NA 1.30; Nikon Instruments), 1.5× magnifier, and iXon EMCCD camera. Focus was maintained using the Perfect Focus System. Movies were analyzed in ImageJ as follows. Secretory vesicle movements were monitored within the mother cells of each strain by manually tracking the positions over time for 5–10 puncta (GFP-Sec4) in each of 10 or more cells. Tortuosity measurements were made by dividing the length of the path (from the initial point of movement to the bud neck) by the distance between the point of origin and the bud neck. For measuring Pearson's correlation for colocalization of Bud6-mCherry and/or GFP-tagged membrane markers (described previously), yeast cells were grown to mid-log phase in synthetic selective media, mounted on slides with coverslips, and immedi-

ately imaged at ambient temperature on an i-E upright confocal microscope equipped with a CSU-W1 spinning disk head, 100× oil objective (NA 1.4; Nikon Instruments), and an Ixon 897 Ultra-CCD camera controlled by NIS-Elements software. Individual cells from each strain were cropped, background removed by subtracting the mean fluorescence in each channel, and colocalization was analyzed by the Coloc2 plugin in ImageJ.

Density of Bud6-mCherry staining in cells at different stages of bud growth (Fig. 6 F) was determined by live imaging on an i-E confocal microscope as above. The outlines of individual cells were traced in ImageJ, and total fluorescence in each cell was measured and then divided by cell area. To quantify levels of Hof1-GFP and Bnr1-GFP at the neck, cells were grown in synthetic media to log phase as above. Then, cells were exposed to 1 µM α-factor (United Biochemical Research Inc.) for 3 h to synchronize cultures (as unbudded cells). Cells were then released from α factor by washing three times in 5 ml synthetic media and resuspended in 100 µl synthetic media. 3–5 µl of this culture was mounted on top of an agarose plug (synthetic media plus 0.7% agarose) on a glass slide. A coverslip was placed on top of the agarose plug and sealed with nail polish. Cells were imaged every 10 min using FITC LED light on a Ti-2 SIM-E inverted microscope with a Hamamatsu Orca Flash 4.0 camera controlled by NIS-Elements software.

Fixed-cell imaging and analysis

Yeast cells were grown to mid-log phase (OD_{600} 0.4–0.6) in YEPD media, then fixed in 4.7% formaldehyde for 45 min, and washed three times with PBS. Cells were stained overnight with Alexa Fluor 488 phalloidin (Life Technologies) and then washed twice with PBS. For experiments in which actin patches were removed, cells were treated with 100 µM CK666 for 10–15 min at 25°C before fixation. For comparing actin cable levels in *myo2-66* and wild-type cells at elevated temperature, cells were grown to mid-log phase as above and then shifted to 35°C for 5 min, fixed, and stained for F-actin as above. Fixed cells were imaged in PBS at ambient temperature by SIM on a Ti-2 SIM-E inverted microscope with a 100× oil objective (NA 1.49), and Hamamatsu Orca Flash 4.0 camera controlled by NIS-Elements software. From SIM images, individual cells were cropped, background was subtracted from maximum intensity images in ImageJ, and actin cables were analyzed using an open source program for biopolymer networks, SOAX (Xu et al., 2015). For all SOAX analyses, default settings were used, with two exceptions, to optimize detection of cables: R-threshold value was set to 0.005 and k-stretch factor was set to 1.0. The number of actin cable segments and intersections, as well as cable orientation maps (relative to the mother-bud axis), was automatically generated. For CV analysis and quantification of actin cable levels in the bud relative to total cellular levels, cables were imaged by confocal microscopy, enabling a larger number of cells to be analyzed. Confocal imaging was performed on an i-E upright microscope equipped with a CSU-W1 spinning disk head, 100× oil objective (NA 1.4) and an Ixon 897 Ultra-CCD camera controlled by NIS-Elements software. To produce CV measurements from confocal images, the standard deviation of fluorescence in a cellular compartment was divided by the mean fluorescence in that compartment. To compare actin cable levels in *myo2-66* and wild-type cells, individual cables in summed projections of mother cells (10 cells per strain) were traced in ImageJ using a line that encompassed the entire width of the cable, and the total fluorescence of each cable was measured. For each mother cell, its sum cable intensity was divided by the mother cell area.

Single-particle EM

Each of four polypeptides was individually imaged by transmission EM after negative staining at the following final concentrations: 500 nM Hof1-FL, 500 nM each Hof1 F-BAR, 200 nM C-Bnr1 (FH1-FH2-C), and 200 nM Bnr1 (FH2). In addition, complexes were imaged after brief mixing of the following polypeptides at the same final concentrations as above: Hof1-FL + C-Bnr1 and Hof1 F-BAR + Bnr1 (FH2). Proteins were applied to carbon-coated glow-discharged transmission EM grids, stained with 0.75% uranyl formate two times for 30 s each, air dried, and imaged on a JEOL 2100 transmission EM. Images were captured using an Ultrascan 1000XP CCD camera (Gatan Inc.) at 40,000× magnification and 1.5–1.9 µm defocus. For the complexes, 80 images (fields of view) were recorded for Hof1 F-BAR + Bnr1 (FH2) and 180 images for Hof1-FL + C-Bnr1. Image processing and 3D reconstruction were performed using EMAN2 (Tang et al., 2007) and Relion-2.0 (Kimanius et al., 2016). 2D class averages were produced by classification in Relion-2.0 of 3,000 untilted images of Hof1-FL + C-Bnr1 particles and 2,500 untilted images of Hof1 F-BAR + Bnr1 (FH2) particles. For each complex, 50 classes were produced, and 25 iterations were used to increase the signal to noise ratio. After classification, all classes were ranked according to quality. The worst classes (representing ∼5% of all particles) were discarded due to low quality. 2D difference mapping was done in IMAGIC (van Heel et al., 1996).

A 3D reconstruction of the Hof1-FL + C-Bnr1 complex was built in EMAN2 using the random conical tilt method. 1,000 particles were selected from 40 pairs of images (at 0° and 45° angles). Untilted images were corrected for the microscope contrast transfer function to account for distortions and classified into five classes. The three classes with the largest number of particles and highest signal to noise were chosen for 3D model building. One model was chosen for further refinement, for which an additional 100 untilted images were acquired. In total, 4,650 particles were subjected to 3D refinement in Relion-2.0. The resolution of the final structure was 10 Å. C1 symmetry was used for the final reconstruction. To generate a 3D reconstruction of the Hof1 F-BAR + Bnr1 (FH2) complex, we collected 40 pairs of tilted and untilted images and processed them as above. After calculating the preliminary 3D reconstruction, 2,500 untilted particles were added to the set. 3,500 particles were used for the final reconstruction, with C1 symmetry. The resolution was 24 Å. To interpret these structures, we fit the atomic structures of the Hof1 F-BAR domain and formin FH2 domain (Protein Data Bank accession numbers 4WPE and 1UX5, respectively) into our density maps using UCSF Chimera.

Statistical analysis

For comparisons of two categories (Figs. 3 E, 7 C, S1 B, and S3 B), an unpaired two-tailed *t* test was used. For comparisons of

more than two categories (Fig. 1 F; Fig. 3, B–F; Fig. 4 C; Fig. 5, D–G; Figs. 6 B; Fig. S1 D; Fig. S4, A and B; and Fig. S5, A–C), one-way ANOVA was applied. Normal distributions were assumed but not formally tested. Error bars in all panels are SEM. In all cases, n.s. indicates not significant; *, $P \le 0.05$; **, $P \le 0.01$; ***, $P \le 0.001$; and ****, $P \le 0.0001$.

Online supplemental material

Fig. S1 shows representative snapshots of TIRF reactions and supporting data for actin assembly assays. Fig. S2 shows supporting EM data on Hof1(F-BAR), Bnr1(FH2), and the complex of both proteins. Fig. S3 shows supporting data for the in vivo analysis of *hof1ΔFBAR* cells, including epifluorescence imaging of Hof1 localization, SIM imaging of actin organization, and cell growth assays. Fig. S4 shows supporting data for TIRF actin assembly assays with reactions containing Bnr1, Hof1, and/or Bud6. Fig. S5 shows additional analysis of actin organization in wild-type, *hof1Δ*, *bud6Δ*, and *hof1Δbud6Δ* cells, as well as representative images from dual-color live imaging of Bud6-mCherry and various GFP-tagged cellular compartments.

Acknowledgments

We are grateful to Erfei Bi for sharing key reagents, Dimitrios Vavylonis and Ting Xu (Lehigh University) for guidance on SOAX analysis, Gonen Memisoglu and James Haber (Brandeis University) for assistance with CRISPR, and the User Facility Center for Electron Microscopy in Life Sciences at Moscow State University. In addition, we thank Julian Eskin, Siyang Guo, Adam Johnston, M. Angeles Juanes, Thomas Rands, and Shashank Shekhar for comments on the manuscript.

This work was supported by the National Institutes of Health (grant R01-GM083137) to B.L. Goode and the Brandeis National Science Foundation Materials Research Science and Engineering Center (grant DMR-1420382). O.S. Sokolova was supported by the Russian Science Foundation (grant 14-14-00234), and T. Stanishneva-Konovalova was supported by the Council on grants of the President of the Russian Federation (grant MK-2614.2018.4).

The authors declare no competing financial interests.

Author contributions: M.V. Garabedian and B.L. Goode designed the study and the experiments. M.V. Garabedian, C. Lou, T.J. Rands, and L.W. Pollard performed and analyzed the experiments. T. Stanishneva-Konovalova and O.S. Sokolova performed and supervised the EM imaging. M.V. Garabedian and B.L. Goode wrote the manuscript.

Submitted: 28 March 2018
Revised: 20 June 2018
Accepted: 17 July 2018

References

Amberg, D.C., J.E. Zahner, J.W. Mulholland, J.R. Pringle, and D. Botstein. 1997. Aip3p/Bud6p, a yeast actin-interacting protein that is involved in morphogenesis and the selection of bipolar budding sites. *Mol. Biol. Cell.* 8:729–753. https://doi.org/10.1091/mbc.8.4.729

Anand, R., G. Memisoglu, and J. Haber. 2017. Cas9-mediated gene editing in Saccharomyces cerevisiae. Protocal Exchange. https://doi.org/10.1038/protex.2017.021a

Aspenström, P., N. Richnau, and A.S. Johansson. 2006. The diaphanous-related formin DAAM1 collaborates with the Rho GTPases RhoA and Cdc42, CIP4 and Src in regulating cell morphogenesis and actin dynamics. *Exp. Cell Res.* 312:2180–2194. https://doi.org/10.1016/j.yexcr.2006.03.013

Blondel, M., S. Bach, S. Bamps, J. Dobbelaere, P. Wiget, C. Longaretti, Y. Barral, L. Meijer, and M. Peter. 2005. Degradation of Hof1 by SCF(Grr1) is important for actomyosin contraction during cytokinesis in yeast. *EMBO J.* 24:1440–1452. https://doi.org/10.1038/sj.emboj.7600627

Breitsprecher, D., and B.L. Goode. 2013. Formins at a glance. *J. Cell Sci.* 126:1–7. https://doi.org/10.1242/jcs.107250

Breitsprecher, D., R. Jaiswal, J.P. Bombardier, C.J. Gould, J. Gelles, and B.L. Goode. 2012. Rocket launcher mechanism of collaborative actin assembly defined by single-molecule imaging. *Science.* 336:1164–1168. https://doi.org/10.1126/science.1218062

Burke, T.A., J.R. Christensen, E. Barone, C. Suarez, V. Sirotkin, and D.R. Kovar. 2014. Homeostatic actin cytoskeleton networks are regulated by assembly factor competition for monomers. *Curr. Biol.* 24:579–585. https://doi.org/10.1016/j.cub.2014.01.072

Buttery, S.M., S. Yoshida, and D. Pellman. 2007. Yeast formins Bni1 and Bnr1 utilize different modes of cortical interaction during the assembly of actin cables. *Mol. Biol. Cell.* 18:1826–1838. https://doi.org/10.1091/mbc.e06-09-0820

Buttery, S.M., K. Kono, E. Stokasimov, and D. Pellman. 2012. Regulation of the formin Bnr1 by septins anda MARK/Par1-family septin-associated kinase. *Mol. Biol. Cell.* 23:4041–4053. https://doi.org/10.1091/mbc.e12-05-0395

Calero, M., C.Z. Chen, W. Zhu, N. Winand, K.A. Havas, P.M. Gilbert, C.G. Burd, and R.N. Collins. 2003. Dual prenylation is required for Rab protein localization and function. *Mol. Biol. Cell.* 14:1852–1867. https://doi.org/10.1091/mbc.e02-11-0707

Carnahan, R.H., and K.L. Gould. 2003. The PCH family protein, Cdc15p, recruits two F-actin nucleation pathways to coordinate cytokinetic actin ring formation in Schizosaccharomyces pombe. *J. Cell Biol.* 162:851–862. https://doi.org/10.1083/jcb.200305012

Chesarone, M., C.J. Gould, J.B. Moseley, and B.L. Goode. 2009. Displacement of formins from growing barbed ends by bud14 is critical for actin cable architecture and function. *Dev. Cell.* 16:292–302. https://doi.org/10.1016/j.devcel.2008.12.001

Chesarone, M.A., A.G. DuPage, and B.L. Goode. 2010. Unleashing formins to remodel the actin and microtubule cytoskeletons. *Nat. Rev. Mol. Cell Biol.* 11:62–74. https://doi.org/10.1038/nrm2816

Chesarone-Cataldo, M., C. Guérin, J.H. Yu, R. Wedlich-Söldner, L. Blanchoin, and B.L. Goode. 2011. The myosin passenger protein Smy1 controls actin cable structure and dynamics by acting as a formin damper. *Dev. Cell.* 21:217–230. https://doi.org/10.1016/j.devcel.2011.07.004

Chhabra, E.S., and H.N. Higgs. 2007. The many faces of actin: matching assembly factors with cellular structures. *Nat. Cell Biol.* 9:1110–1121. https://doi.org/10.1038/ncb1007-1110

Delgehyr, N., C.S. Lopes, C.A. Moir, S.M. Huisman, and M. Segal. 2008. Dissecting the involvement of formins in Bud6p-mediated cortical capture of microtubules in S. cerevisiae. *J. Cell Sci.* 121:3803–3814. https://doi.org/10.1242/jcs.036269

Eisenmann, K.M., E.S. Harris, S.M. Kitchen, H.A. Holman, H.N. Higgs, and A.S. Alberts. 2007. Dia-interacting protein modulates formin-mediated actin assembly at the cell cortex. *Curr. Biol.* 17:579–591. https://doi.org/10.1016/j.cub.2007.03.024

Eskin, J.A., A. Rankova, A.B. Johnston, S.L. Alioto, and B.L. Goode. 2016. Common formin-regulating sequences in Smy1 and Bud14 are required for the control of actin cable assembly in vivo. *Mol. Biol. Cell.* 27:828–837. https://doi.org/10.1091/mbc.e15-09-0639

Evangelista, M., K. Blundell, M.S. Longtine, C.J. Chow, N. Adames, J.R. Pringle, M. Peter, and C. Boone. 1997. Bni1p, a yeast formin linking cdc42p and the actin cytoskeleton during polarized morphogenesis. *Science.* 276:118–122. https://doi.org/10.1126/science.276.5309.118

Evangelista, M., D. Pruyne, D.C. Amberg, C. Boone, and A. Bretscher. 2002. Formins direct Arp2/3-independent actin filament assembly to polarize cell growth in yeast. *Nat. Cell Biol.* 4:260–269. https://doi.org/10.1038/ncb718

Faix, J., and R. Grosse. 2006. Staying in shape with formins. *Dev. Cell.* 10:693–706. https://doi.org/10.1016/j.devcel.2006.05.001

Gao, L., W. Liu, and A. Bretscher. 2010. The yeast formin Bnr1p has two localization regions that show spatially and temporally distinct association with septin structures. *Mol. Biol. Cell.* 21:1253–1262. https://doi.org/10.1091/mbc.e09-10-0861

Goode, B.L., and M.J. Eck. 2007. Mechanism and function of formins in the control of actin assembly. *Annu. Rev. Biochem.* 76:593–627. https://doi.org/10.1146/annurev.biochem.75.103004.142647

Graziano, B.R., A.G. DuPage, A. Michelot, D. Breitsprecher, J.B. Moseley, I. Sagot, L. Blanchoin, and B.L. Goode. 2011. Mechanism and cellular function of Bud6 as an actin nucleation-promoting factor. *Mol. Biol. Cell.* 22:4016–4028. https://doi.org/10.1091/mbc.e11-05-0404

Graziano, B.R., E.M. Jonasson, J.G. Pullen, C.J. Gould, and B.L. Goode. 2013. Ligand-induced activation of a formin-NPF pair leads to collaborative actin nucleation. *J. Cell Biol.* 201:595–611. https://doi.org/10.1083/jcb.201212059

Graziano, B.R., H.-Y.E. Yu, S.L. Alioto, J.A. Eskin, C.A. Ydenberg, D.P. Waterman, M. Garabedian, and B.L. Goode. 2014. The F-BAR protein Hof1 tunes formin activity to sculpt actin cables during polarized growth. *Mol. Biol. Cell.* 25:1730–1743. https://doi.org/10.1091/mbc.e14-03-0850

Guthrie, C., and G.R. Fink. 1991. Guide to yeast genetics and molecular biology. *Methods Enzymol.* 194:1–863.

Henty-Ridilla, J.L., A. Rankova, J.A. Eskin, K. Kenny, and B.L. Goode. 2016. Accelerated actin filament polymerization from microtubule plus ends. *Science.* 352:1004–1009. https://doi.org/10.1126/science.aaf1709

Huisman, S.M., O.A. Bales, M. Bertrand, M.F. Smeets, S.I. Reed, and M. Segal. 2004. Differential contribution of Bud6p and Kar9p to microtubule capture and spindle orientation in S. cerevisiae. *J. Cell Biol.* 167:231–244. https://doi.org/10.1083/jcb.200407167

Hurley, J.H. 2006. Membrane binding domains. *Biochim. Biophys. Acta.* 1761:805–811. https://doi.org/10.1016/j.bbalip.2006.02.020

Jaiswal, R., D. Breitsprecher, A. Collins, I.R. Corrêa Jr., M.-Q. Xu, and B.L. Goode. 2013. The formin Daam1 and fascin directly collaborate to promote filopodia formation. *Curr. Biol.* 23:1373–1379. https://doi.org/10.1016/j.cub.2013.06.013

Jimbo, T., Y. Kawasaki, R. Koyama, R. Sato, S. Takada, K. Haraguchi, and T. Akiyama. 2002. Identification of a link between the tumour suppressor APC and the kinesin superfamily. *Nat. Cell Biol.* 4:323–327. https://doi.org/10.1038/ncb779

Jin, H., and D.C. Amberg. 2000. The secretory pathway mediates localization of the cell polarity regulator Aip3p/Bud6p. *Mol. Biol. Cell.* 11:647–661. https://doi.org/10.1091/mbc.11.2.647

Johnston, G.C., J.A. Prendergast, and R.A. Singer. 1991. The Saccharomyces cerevisiae MYO2 gene encodes an essential myosin for vectorial transport of vesicles. *J. Cell Biol.* 113:539–551. https://doi.org/10.1083/jcb.113.3.539

Juanes, M.A., H. Bouguenina, J.A. Eskin, R. Jaiswal, A. Badache, and B.L. Goode. 2017. Adenomatous polyposis coli nucleates actin assembly to drive cell migration and microtubule-induced focal adhesion turnover. *J. Cell Biol.* 216:2859–2875.

Kamei, T., K. Tanaka, T. Hihara, M. Umikawa, H. Imamura, M. Kikyo, K. Ozaki, and Y. Takai. 1998. Interaction of Bnr1p with a novel Src homology 3 domain-containing Hof1p. Implication in cytokinesis in Saccharomyces cerevisiae. *J. Biol. Chem.* 273:28341–28345. https://doi.org/10.1074/jbc.273.43.28341

Kast, D.J., C. Yang, A. Disanza, M. Boczkowska, Y. Madasu, G. Scita, T. Svitkina, and R. Dominguez. 2014. Mechanism of IRSp53 inhibition and combinatorial activation by Cdc42 and downstream effectors. *Nat. Struct. Mol. Biol.* 21:413–422. https://doi.org/10.1038/nsmb.2781

Kelley, C.F., E.M. Messelaar, T.L. Eskin, S. Wang, K. Song, K. Vishnia, A.N. Becalska, O. Shupliakov, M.F. Hagan, D. Danino, et al. 2015. Membrane Charge Directs the Outcome of F-BAR Domain Lipid Binding and Autoregulation. *Cell Reports.* 13:2597–2609. https://doi.org/10.1016/j.celrep.2015.11.044

Kimanius, D., B.O. Forsberg, S.H. Scheres, and E. Lindahl. 2016. Accelerated cryo-EM structure determination with parallelisation using GPUs in RELION-2. *eLife.* 5:e18722. https://doi.org/10.7554/eLife.18722

Kita, K., T. Wittmann, I.S. Näthke, and C.M. Waterman-Storer. 2006. Adenomatous polyposis coli on microtubule plus ends in cell extensions can promote microtubule net growth with or without EB1. *Mol. Biol. Cell.* 17:2331–2345. https://doi.org/10.1091/mbc.e05-06-0498

Kovar, D.R. 2006. Molecular details of formin-mediated actin assembly. *Curr. Opin. Cell Biol.* 18:11–17. https://doi.org/10.1016/j.ceb.2005.12.011

Liu, H., and A. Bretscher. 1992. Characterization of TPM1 disrupted yeast cells indicates an involvement of tropomyosin in directed vesicular transport. *J. Cell Biol.* 118:285–299. https://doi.org/10.1083/jcb.118.2.285

Longtine, M.S., A. McKenzie III, D.J. Demarini, N.G. Shah, A. Wach, A. Brachat, P. Philippsen, and J.R. Pringle. 1998. Additional modules for versatile and economical PCR-based gene deletion and modification in Saccharomyces cerevisiae. *Yeast.* 14:953–961. https://doi.org/10.1002/(SICI)1097-0061(199807)14:10%3C953::AID-YEA293%3E3.0.CO;2-U

Maiti, S., A. Michelot, C. Gould, L. Blanchoin, O. Sokolova, and B.L. Goode. 2012. Structure and activity of full-length formin mDia1. *Cytoskeleton (Hoboken).* 69:393–405. https://doi.org/10.1002/cm.21033

Martin, S.G., S.A. Rincón, R. Basu, P. Pérez, and F. Chang. 2007. Regulation of the formin for3p by cdc42p and bud6p. *Mol. Biol. Cell.* 18:4155–4167. https://doi.org/10.1091/mbc.e07-02-0094

Mason, F.M., E.G. Heimsath, H.N. Higgs, and S.H. Soderling. 2011. Bi-modal regulation of a formin by srGAP2. *J. Biol. Chem.* 286:6577–6586. https://doi.org/10.1074/jbc.M110.190397

McDonald, N.A., and K.L. Gould. 2016. Linking up at the BAR: Oligomerization and F-BAR protein function. *Cell Cycle.* 15:1977–1985. https://doi.org/10.1080/15384101.2016.1190893

McDonald, N.A., Y. Takizawa, A. Feoktistova, P. Xu, M.D. Ohi, C.W. Vander Kooi, and K.L. Gould. 2016. The Tubulation Activity of a Fission Yeast F-BAR Protein Is Dispensable for Its Function in Cytokinesis. *Cell Reports.* 14:534–546. https://doi.org/10.1016/j.celrep.2015.12.062

Meitinger, F., M.E. Boehm, A. Hofmann, B. Hub, H. Zentgraf, W.D. Lehmann, and G. Pereira. 2011. Phosphorylation-dependent regulation of the F-BAR protein Hof1 during cytokinesis. *Genes Dev.* 25:875–888. https://doi.org/10.1101/gad.622411

Meitinger, F., S. Palani, B. Hub, and G. Pereira. 2013. Dual function of the NDR-kinase Dbf2 in the regulation of the F-BAR protein Hof1 during cytokinesis. *Mol. Biol. Cell.* 24:1290–1304. https://doi.org/10.1091/mbc.e12-08-0608

Mimori-Kiyosue, Y., N. Shiina, and S. Tsukita. 2000. Adenomatous polyposis coli (APC) protein moves along microtubules and concentrates at their growing ends in epithelial cells. *J. Cell Biol.* 148:505–518. https://doi.org/10.1083/jcb.148.3.505

Mohapatra, L., B.L. Goode, and J. Kondev. 2015. Antenna Mechanism of Length Control of Actin Cables. *PLOS Comput. Biol.* 11:e1004160. https://doi.org/10.1371/journal.pcbi.1004160

Moravcevic, K., D. Alvarado, K.R. Schmitz, J.A. Kenniston, J.M. Mendrola, K.M. Ferguson, and M.A. Lemmon. 2015. Comparison of Saccharomyces cerevisiae F-BAR domain structures reveals a conserved inositol phosphate binding site. *Structure.* 23:352–363. https://doi.org/10.1016/j.str.2014.12.009

Moseley, J.B., and B.L. Goode. 2005. Differential activities and regulation of Saccharomyces cerevisiae formin proteins Bni1 and Bnr1 by Bud6. *J. Biol. Chem.* 280:28023–28033. https://doi.org/10.1074/jbc.M503094200

Moseley, J.B., and B.L. Goode. 2006. The yeast actin cytoskeleton: from cellular function to biochemical mechanism. *Microbiol. Mol. Biol. Rev.* 70:605–645. https://doi.org/10.1128/MMBR.00013-06

Moseley, J.B., S. Maiti, and B.L. Goode. 2006. Formin proteins: purification and measurement of effects on actin assembly. *Methods Enzymol.* 406:215–234. https://doi.org/10.1016/S0076-6879(06)06016-2

Nishihama, R., J.H. Schreiter, M. Onishi, E.A. Vallen, J. Hanna, K. Moravcevic, M.F. Lippincott, H. Han, M.A. Lemmon, J.R. Pringle, and E. Bi. 2009. Role of Inn1 and its interactions with Hof1 and Cyk3 in promoting cleavage furrow and septum formation in S. cerevisiae. *J. Cell Biol.* 185:995–1012. https://doi.org/10.1083/jcb.200903125

Nkosi, P.J., B.S. Targosz, K. Labib, and A. Sanchez-Diaz. 2013. Hof1 and Rvs167 have redundant roles in actomyosin ring function during cytokinesis in budding yeast. *PLoS One.* 8:e57846. https://doi.org/10.1371/journal.pone.0057846

Nolen, B.J., N. Tomasevic, A. Russell, D.W. Pierce, Z. Jia, C.D. McCormick, J. Hartman, R. Sakowicz, and T.D. Pollard. 2009. Characterization of two classes of small molecule inhibitors of Arp2/3 complex. *Nature.* 460:1031–1034. https://doi.org/10.1038/nature08231

Oh, Y., J. Schreiter, R. Nishihama, C. Wloka, and E. Bi. 2013. Targeting and functional mechanisms of the cytokinesis-related F-BAR protein Hof1 during the cell cycle. *Mol. Biol. Cell.* 24:1305–1320. https://doi.org/10.1091/mbc.e12-11-0804

Okada, K., F. Bartolini, A.M. Deaconescu, J.B. Moseley, Z. Dogic, N. Grigorieff, G.G. Gundersen, and B.L. Goode. 2010. Adenomatous polyposis coli protein nucleates actin assembly and synergizes with the formin mDia1. *J. Cell Biol.* 189:1087–1096. https://doi.org/10.1083/jcb.201001016

Park, E., B.R. Graziano, W. Zheng, M. Garabedian, B.L. Goode, and M.J. Eck. 2015. Structure of a Bud6/Actin Complex Reveals a Novel WH2-like Actin Monomer Recruitment Motif. *Structure.* 23:1492–1499. https://doi.org/10.1016/j.str.2015.05.015

Pollard, T.D., and J.A. Cooper. 1984. Quantitative analysis of the effect of Acanthamoeba profilin on actin filament nucleation and elongation. *Biochemistry.* 23:6631–6641. https://doi.org/10.1021/bi00321a054

Pruyne, D., M. Evangelista, C. Yang, E. Bi, S. Zigmond, A. Bretscher, and C. Boone. 2002. Role of formins in actin assembly: nucleation and barbed-end association. *Science.* 297:612–615. https://doi.org/10.1126/science.1072309

Pruyne, D., L. Gao, E. Bi, and A. Bretscher. 2004. Stable and dynamic axes of polarity use distinct formin isoforms in budding yeast. *Mol. Biol. Cell.* 15:4971–4989. https://doi.org/10.1091/mbc.e04-04-0296

Quinlan, M.E. 2013. Direct interaction between two actin nucleators is required in Drosophila oogenesis. *Development.* 140:4417–4425. https://doi.org/10.1242/dev.097337

Rao, Y., Q. Ma, A. Vahedi-Faridi, A. Sundborger, A. Pechstein, D. Puchkov, L. Luo, O. Shupliakov, W. Saenger, and V. Haucke. 2010. Molecular basis for SH3 domain regulation of F-BAR-mediated membrane deformation. *Proc. Natl. Acad. Sci. USA.* 107:8213–8218. https://doi.org/10.1073/pnas.1003478107

Ruane, P.T., L.F. Gumy, B. Bola, B. Anderson, M.J. Wozniak, C.C. Hoogenraad, and V.J. Allan. 2016. Tumour Suppressor Adenomatous Polyposis Coli (APC) localisation is regulated by both Kinesin-1 and Kinesin-2. *Sci. Rep.* 6:27456. https://doi.org/10.1038/srep27456

Sagot, I., S.K. Klee, and D. Pellman. 2002a. Yeast formins regulate cell polarity by controlling the assembly of actin cables. *Nat. Cell Biol.* 4:42–50. https://doi.org/10.1038/ncb719

Sagot, I., A.A. Rodal, J. Moseley, B.L. Goode, and D. Pellman. 2002b. An actin nucleation mechanism mediated by Bni1 and profilin. *Nat. Cell Biol.* 4:626–631. https://doi.org/10.1038/ncb834

Sambrook, J., E.F. Fritsch, and T. Maniatis. 1989. Molecular Cloning: A Laboratory Manual. Cold Spring Harbor Laboratory Press, Cold Spring Harbor, NY.

Schott, D., J. Ho, D. Pruyne, and A. Bretscher. 1999. The COOH-terminal domain of Myo2p, a yeast myosin V, has a direct role in secretory vesicle targeting. *J. Cell Biol.* 147:791–808. https://doi.org/10.1083/jcb.147.4.791

Schott, D.H., R.N. Collins, and A. Bretscher. 2002. Secretory vesicle transport velocity in living cells depends on the myosin-V lever arm length. *J. Cell Biol.* 156:35–39. https://doi.org/10.1083/jcb.200110086

Segal, M., K. Bloom, and S.I. Reed. 2000. Bud6 directs sequential microtubule interactions with the bud tip and bud neck during spindle morphogenesis in Saccharomyces cerevisiae. *Mol. Biol. Cell.* 11:3689–3702. https://doi.org/10.1091/mbc.11.11.3689

Segal, M., K. Bloom, and S.I. Reed. 2002. Kar9p-independent microtubule capture at Bud6p cortical sites primes spindle polarity before bud emergence in Saccharomyces cerevisiae. *Mol. Biol. Cell.* 13:4141–4155. https://doi.org/10.1091/mbc.02-05-0067

Spudich, J.A., and S. Watt. 1971. The regulation of rabbit skeletal muscle contraction. I. Biochemical studies of the interaction of the tropomyosin-troponin complex with actin and the proteolytic fragments of myosin. *J. Biol. Chem.* 246:4866–4871.

Stanishneva-Konovalova, T.B., C.F. Kelley, T.L. Eskin, E.M. Messelaar, S.A. Wasserman, O.S. Sokolova, and A.A. Rodal. 2016. Coordinated autoinhibition of F-BAR domain membrane binding and WASp activation by Nervous Wreck. *Proc. Natl. Acad. Sci. USA.* 113:E5552–E5561. https://doi.org/10.1073/pnas.1524412113

Tang, G., L. Peng, P.R. Baldwin, D.S. Mann, W. Jiang, I. Rees, and S.J. Ludtke. 2007. EMAN2: an extensible image processing suite for electron microscopy. *J. Struct. Biol.* 157:38–46. https://doi.org/10.1016/j.jsb.2006.05.009

Ten Hoopen, R., C. Cepeda-García, R. Fernández-Arruti, M.A. Juanes, N. Delgehyr, and M. Segal. 2012. Mechanism for astral microtubule capture by cortical Bud6p priming spindle polarity in S. cerevisiae. *Curr. Biol.* 22:1075–1083. https://doi.org/10.1016/j.cub.2012.04.059

Tu, D., B.R. Graziano, E. Park, W. Zheng, Y. Li, B.L. Goode, and M.J. Eck. 2012. Structure of the formin-interaction domain of the actin nucleation-promoting factor Bud6. *Proc. Natl. Acad. Sci. USA.* 109:E3424–E3433. https://doi.org/10.1073/pnas.1203035109

Vallen, E.A., J. Caviston, and E. Bi. 2000. Roles of Hof1p, Bni1p, Bnr1p, and myo1p in cytokinesis in Saccharomyces cerevisiae. *Mol. Biol. Cell.* 11:593–611. https://doi.org/10.1091/mbc.11.2.593

van Heel, M., G. Harauz, E.V. Orlova, R. Schmidt, and M. Schatz. 1996. A new generation of the IMAGIC image processing system. *J. Struct. Biol.* 116:17–24. https://doi.org/10.1006/jsbi.1996.0004

Wang, M., R. Nishihama, M. Onishi, and J.R. Pringle. 2018. Role of the Hof1-Cyk3 interaction in cleavage-furrow ingression and primary-septum formation during yeast cytokinesis. *Mol. Biol. Cell.* 29:597–609. https://doi.org/10.1091/mbc.E17-04-0227

Willet, A.H., N.A. McDonald, K.A. Bohnert, M.A. Baird, J.R. Allen, M.W. Davidson, and K.L. Gould. 2015. The F-BAR Cdc15 promotes contractile ring formation through the direct recruitment of the formin Cdc12. *J. Cell Biol.* 208:391–399. https://doi.org/10.1083/jcb.201411097

Willet, A.H., K.A. Bohnert, and K.L. Gould. 2018. Cdk1-dependent phosphoinhibition of a formin-F-BAR interaction opposes cytokinetic contractile ring formation. *Mol. Biol. Cell.* 29:713–721. https://doi.org/10.1091/mbc.E17-11-0646

Xu, T., D. Vavylonis, F.C. Tsai, G.H. Koenderink, W. Nie, E. Yusuf, J.Q. I-Ju Lee, Wu, and X. Huang. 2015. SOAX: a software for quantification of 3D biopolymer networks. *Sci. Rep.* 5:9081. https://doi.org/10.1038/srep09081

Xu, Y., J.B. Moseley, I. Sagot, F. Poy, D. Pellman, B.L. Goode, and M.J. Eck. 2004. Crystal structures of a Formin Homology-2 domain reveal a tethered dimer architecture. *Cell.* 116:711–723. https://doi.org/10.1016/S0092-8674(04)00210-7

Yan, S., Z. Lv, M. Winterhoff, C. Wenzl, T. Zobel, J. Faix, S. Bogdan, and J. Grosshans. 2013. The F-BAR protein Cip4/Toca-1 antagonizes the formin Diaphanous in membrane stabilization and compartmentalization. *J. Cell Sci.* 126:1796–1805. https://doi.org/10.1242/jcs.118422

Yang, H.C., and L.A. Pon. 2002. Actin cable dynamics in budding yeast. *Proc. Natl. Acad. Sci. USA.* 99:751–756. https://doi.org/10.1073/pnas.022462899

Yu, J.H., A.H. Crevenna, M. Bettenbühl, T. Freisinger, and R. Wedlich-Söldner. 2011. Cortical actin dynamics driven by formins and myosin V. *J. Cell Sci.* 124:1533–1541. https://doi.org/10.1242/jcs.079038

Zaoui, K., K. Benseddik, P. Daou, D. Salaün, and A. Badache. 2010. ErbB2 receptor controls microtubule capture by recruiting ACF7 to the plasma membrane of migrating cells. *Proc. Natl. Acad. Sci. USA.* 107:18517–18522. https://doi.org/10.1073/pnas.1000975107